UNITED NATIONS UNIVERSITY
UNU-GTP
Geothermal Training Programme

Orkustofnun, Grensasvegur 9,
IS-108 Reykjavik, Iceland

Reports 2014
Number 8

EVALUATION OF FLUID - MINERAL INTERACTION IN THE MENENGAI GEOTHERMAL SYSTEM, CENTRAL RIFT, KENYA

Leakey Ochieng Auko
Geothermal Development Company - GDC
P.O. Box 17700-20100
Nakuru
KENYA
lochieng@gdc.co.ke, leakeyochieng@gmail.com

ABSTRACT

The geothermal reservoir fluid composition, water-rock interaction and possible causes of excess enthalpy were studied in the Menengai geothermal system, Kenya. The reservoir fluid composition and aqueous speciation distribution were assessed based on two models: first assuming that the excess enthalpy was caused by two-phase reservoir fluids (water and vapour) and, secondly, assuming single liquid phase reservoir fluids. The calculated chemical composition of major non-volatile components is relatively similar in both models except when the well discharges approach dry steam. The concentration of the volatiles in reservoir water is significantly lower when assuming a liquid and vapour reservoir and higher when assuming a liquid only reservoir. For these reasons, H_2S geothermometers give significantly lower values when assuming a two-phase reservoir. Moreover, the geothermometer temperatures show a remarkable discrepancy as a result of mixing of fluids from different feed zones that may affect the fluid equilibrium at a given temperature. The exception to this is for wells where the discharges approach dry steam. While there is some uncertainty due to the model calculations, virtually all the common Ca-bearing minerals observed in Menengai are under-saturated. However, andradite and epidote, which also contain Fe (III), show mixed saturation states, whereas Fe (II) bearing minerals are oversaturated; this might be affected by the calculated Fe activity that is sensitive to precipitation and dissolution. Menengai aquifer waters are saturated with respect to albites and K-feldspars. The calculated activity of volatiles in the aquifer water in relation to mineral buffers is model-type dependent. Therefore, activities of the volatiles are close to equilibrium with volatile mineral buffers when assuming two-phase reservoir fluids, while a departure is observed when assuming a liquid reservoir. The trends displayed by the non-volatile Cl concentration in the total well discharge and in the liquid phase as a function of discharge enthalpy suggests that Menengai has a heterogeneous reservoir, with excess enthalpy predominantly caused by phase separation and conductive heat transfer from hot rock or magma to the circulating fluids, also compounding to form superheated steam.

1. INTRODUCTION

Geochemistry in the context of geothermal systems is a multifaceted geoscience that takes into account various physical and chemical processes under different geological conditions. The physical processes include heat and mass transfer, temperature-pressure gradients, permeability and porosity and hydrological fluid flow, just to name a few. The chemical processes include fluid composition, the source of the fluid and fluid-rock interaction. This study focuses on the geochemistry of the Menengai geothermal system, located in the central segment of the Kenya Rift Valley (Figure 1). Development of the field is underway with the primary goal of generating electricity. So far wells have been drilled into the liquid-dominated high temperature geothermal reservoir, most of which have discharged two-phase fluids. However, some wells have discharge enthalpy corresponding to vapour-dominated conditions in the reservoir and have discharged single-phase vapour only.

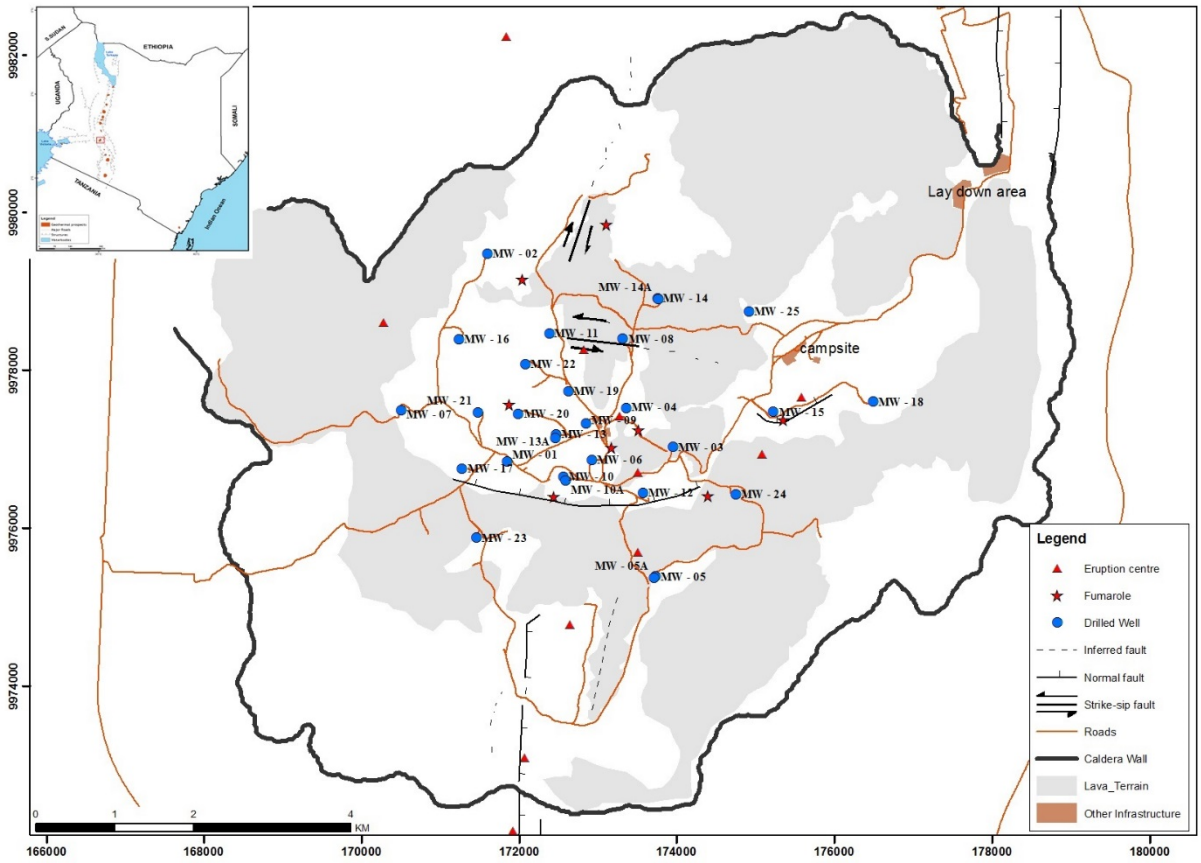

FIGURE 1: Location map of Menengai geothermal field

Previously it was established that the chemistry of the fluids discharged from the Menengai wells was of Na-HCO_3 type (Kipng'ok, 2011; Sekento, 2012; ELC, 2013; Malimo, 2013). The fluid composition of well discharges at the surface is variable, particularly with respect to volatile concentrations. The causes of such variability may be many, including heterogenic reservoir composition and phase predominance (liquid dominated or two phase reservoir fluids) but also boiling induced by heat addition or phase segregation, both of which would lead to increased measured discharge enthalpy at the surface (Arnórsson et al., 2007).

In this study the geothermal reservoir fluid composition, water-rock interaction, and possible causes of discharge excess enthalpy were studied in the Menengai geothermal system, Kenya. The study report was carried out in partial fulfilment of the requirements of the six month diploma course at the United Nations University Geothermal Training Programme (UNU-GTP) with a specialisation in the field of chemistry of thermal fluids.

2. GEOLOGY AND GEOTHERMAL ACTIVITY

2.1 Geology

Menengai is an elliptical piecemeal caldera of the Krakatau-style, formed through different episodes of collapse that are associated with two major eruptions, thus leading to the partly superposed lava flows of different ages. The lava flow covers virtually the entire caldera floor (Figure 1). The rocks conform to the pre-, syn- and post caldera volcanic activities that started about 0.18 Ma (UP and GDC, 2013; Leat, 1984). The surface and subsurface geology of Menengai geothermal field is predominantly trachytic with intercalations of tuff and pyroclastics. Pulses of trachyphonolite are reported to be present in Menengai. Studies of drill cuttings from various wells have also revealed lenses of syenitic intrusions. The varying texture of the trachytes and the intermittent tuff intercepted reflect different eruption episodes. In addition, the highly altered basalt penetrated by some wells at greater depths is presumed to be older than the caldera and could correspond to pre-caldera volcanics that date about mid to late Pleistocene. Geothermal activity manifests on the surface in the form of weak fumaroles, steaming grounds and steam vents, most of which are structurally controlled (Mbia, 2014; Kipchumba, 2013; Lopeyok, 2013; UP and GDC, 2013; Mibei and Lagat, 2012; Omondi, 2011).

Mibei and Lagat (2011) grouped the structural systems in the Menengai field into caldera ring structures, a Molo tectono-volcanic axis, a solai graben and dominant NNW-SSE, NNE-SSW trending faults and fractures. On a regional scale, Menengai caldera is exclusively affected by NNE-SSW striking normal fault kinematics cutting the caldera rim to the north of the Ol' rongai and Solai and Makalia fault system which forms the fissure zone, and the aligned craters north of Ronda Hill to the south, while the western sectors appear to be unaffected. In addition, at the northern rim, the NNE oriented Solai graben cuts the caldera rim, but this fault system is subdued and, therefore, cannot be traced further into the caldera (UP and GDC, 2013; Mibei and Lagat, 2012; Leat, 1984).

UP and GDC (2013) suggested that it appears likely that the local structures with different fault kinematics in the caldera could have formed as a direct consequence of magmatic injection into the uppermost crust and are independent of the regional tectonic stress field. These local structures are perceived to be responsible for the resurgence in an extensional regime and control fumarolic activity.

The majority of the subsidiary structures inside the caldera floor have different orientations and could demonstrate the possible result of an interference pattern between the regional stress field and a local stress-field perturbance. It is, therefore, postulated that central-caldera structures are incompatible with the remainder of the structural inventory and, thus, are interpreted to reflect a local, magmatically driven stress-field perturbation (UP and GDC, 2013). Simiyu (2009) pointed out that the formation of the resurgent dome at the centre of the caldera could be indicative of on-going magmatic activity at depth; therefore, it is reasonable to assume that magma is at a shallower depth around the summit. This is affirmed by the immense shallow seismic events within the caldera centre, north eastern caldera rim and the Olbanita area which, together, embody the areas overlying the heat sources for the geothermal system. These areas have the lowest average vp/vs ratios, corresponding to depths of around 4.3 – 5 km. The geometry of the heat source is also underpinned by past (Simiyu and Keller, 2001) and recent (GDC, 2014) gravity measurements which indicate an intrusive body at about 4 km depth with high gravity anomalies concentrated at the summit of the caldera. The joint MT and TEM data reflect a low resistivity anomaly, indicating a magma chamber or a heat source at depths greater than 4 km beneath the Menengai geothermal system (Wamalwa, 2013, 2011; Gichira, 2012).

2.2 Hydrology

The surface drainage is mainly focused on the eastern and western parts of the area and the hydrological flow is mainly directed to the north (Mungania, 2014). Permanent rivers within the precincts of Menengai are the Molo and Rongai in the northwest while the ephemeral rivers are

Wanyororo, Crater and Olbanita in the eastern part. The conduits of the closely spaced network of faults, fractures and fissures essentially control the hydrogeological regime of Menengai system, as demonstrated by N-S trending fault/fractures which channel the disappearing stream in the paleo crater-lake region and other areas (Lagat et al., 2010; Sekento, 2012; Mbia, 2014).

In light of the stable deuterium isotopes, the origin of geothermal fluids in Menengai is typically considered to be comprised of meteoric component. The thermal fluids discharged from Menengai reservoir contain H_2O with a δD value in the range of -10 ‰ to -20 ‰ from fumarolic discharge (Geotermica Italiana Srl, 1987) which correlates with a δD value of about -15.7 ‰ for well MW-04 condensate, while its computed deep δD value is about -4.52‰ due to the susceptibility of steam to isotopic fractionation (Sekento, 2012). In addition, Sekento (2012) further established that thermal fluids from Menengai wells MW-01, MW-04 and MW-06 show a mixture of local groundwater and Lake Nakuru waters.

2.3 Hydrothermal alteration mineralogy

The primary mineralogy of the Menengai rocks consists of olivines, pyroxenes, amphiboles, feldspars, volcanic glass and Fe-Ti oxides including ilmenite and magnetite. The main hydrothermal alteration minerals that have been observed in subsurface rock cuttings include: zeolites, chalcedony, quartz, pyrite, calcite, smectite, hematite, illite, albite, actinolite, chalcopyrite, fluorite, pyrrhotite, epidote, wollastonite, titanite (sphene), chlorite, and actinolite (Kahiga, 2014; Kipchumba, 2013; Lopeyok, 2013; Mibei, 2012; Omondi, 2011). The alteration mineralogy shows a depth zonal distribution with progressive depth: (1) zone of no alteration, (2) smectite-zeolite zone, (3) illite-quartz zone; (4) illite-quartz-wollastonite zone and (5) epidote-wollastonite-actinolite-illite zone (Kipchumba, 2013; Lopeyok, 2013; Mibei, 2012).

The occurrence of these minerals could be a function of varying rock composition within the lithostratigraphy of the geothermal system, changes in temperature with time, pulses of magmatic input and a varying degree of water-rock interaction. Multiple studies have demonstrated that various mineral assemblages, presented in Tables 2 and 3, could potentially buffer the concentration of gases CO_2, H_2S and H_2 in the aquifer fluids of the six discharged two-phase wells used in this study. A considerable number of these mineral buffers have been observed in Menengai except for grossular-andradite garnets and prehnite. Nevertheless, prehnite crystals in drill-cuttings are known to be too small for even electron microprobe analysis (<20μm) (Freedman et al., 2010). Therefore, the possibility of prehnite occurrence cannot be discounted. Albeit not discernible in the presently intercepted Menengai rock cuttings, grossular-garnet and prehnite were still considered in order to evaluate the mineral-solution equilibrium, with respect to H_2S and H_2, since they control the concentration of these gases in most volcanic geothermal systems.

3. CHEMICAL DATA BASE AND DATA HANDLING

3.1 Sampling and analysis

Sampling and analysis of water and steam samples were carried out, as previously described in detail by Arnórsson et al. (2006). Collection of steam and water samples was done using a chromium steel Webre separator attached fairly close to the wellhead of each well during a horizontal discharge testing. The liquid samples were collected into polyethylene bottles while the gas samples were collected in pre-weighed 325-340 ml evacuated gas sampling flasks containing 50 ml of 40% w/v NaOH solution to react with the major non-condensable gases (CO_2 and H_2S), while residual gases (CH_4, H_2, N_2 and O_2) occupy the head space. Water samples were treated upon collection, depending on the analysis required. Samples to be used for the determination of pH, TDS, conductivity, total

carbonates carbon (TCC), Cl, F and B were collected and untreated. Samples for SiO_2 analysis were diluted ten times using deionized water to avoid polymerization of monomeric silica. Samples to be analyzed for cations and SO_4 were filtered through a 0.45 µm millipore membrane. Cation samples were preserved with 1 ml nitric acid, while 1 ml of 0.2 M Zn-acetate solution was added to the samples for SO_4 analysis to precipitate the sulphides in the form of ZnS.

An analysis of the water samples for determination of pH, TDS, conductivity, and TCC was done at the Geothermal Development Company (GDC) laboratory a few hours after sampling. Analysis of CO_2 as TCC and H_2S in the water samples was carried out titrimetrically using 0.1M HCl and 0.001M Hg-acetate, respectively, with the H_2S analysis being done on site. Analysis of the major aqueous cation components (Na, K, Ca, Mg, Fe, Al and Li) was done using the AAS. Chloride analysis was done titrimetrically using the argentometric Mohr's method using $AgNO_3$ while fluoride was analysed using ISE. The analysis of B, SiO_2 and SO_4 was done spectrophotometrically using UV/ Vis, using major reagents such as curcumin, ammonium molybdate, and barium chloride, respectively. Steam samples were analysed for CO_2, H_2S, CH_4, H_2, N_2 and O_2. Non-condensable gases (CH_4, H_2, N_2 and O_2) in the head space of the sampling bulb were analysed by using a Shimadzu model gas chromatograph while analysis for CO_2 and H_2S from the NaOH condensate was done titrimetrically in the same way as the water samples. The chemical results are presented in Table 1.

TABLE 1: Chemical composition of well discharges collected at Menengai geothermal field

Well No.	Sample No.	Sampling date	$h^{d,t}$ (kJ/kg)	p^{wh}, bar-g	p^{s}, bar-g	pH/T°C	Liquid phase components (mg/kg)														Vapour phase (mmole/kg)					
							CO_2	H_2S	B	SiO_2	Na	K	Mg	Ca	F	Cl	SO_4	Al	Fe	TDS	CBE^{ic} (%)	CO_2	H_2S	H_2	CH_4	N_2	O_2
MW-12	414	27-Feb-13	1600	8.618	8.27	8.5/23.8	3454	74.8	0.319	302	2327	92	0.27	0.23	64	581.3	291	0.35	0.01	4830	-0.5	4758	50.1	243.7	19.2	29.4	0.00
MW-12	438	25-Mar-13	1492	2.965	2.76	9.0/23.9	4554	91.8	0.214	440	3479	68	3.50	0.03	75	705.5	358	0.27	0.68	5980	4.6	2840	27.9	147.2	14.3	7.8	0.00
MW-12	474	6-May-13	1580	5.861	4.14	8.7/22.9	4579	159.8	0.326	528	3567	116	0.35	0.47	64	908.0	227	0.49	0.28	5820	6.2	2862	33.0	115.8	11.7	4.3	0.0
MW-03	323	12-Nov-12	1267	0.483	0.34	7.6/23.4	4796	18.36	0.396	247	2950	99	3.13	0.27	97	984.9	355	0.85	0.78	6210	-4.7	906	2.4	5.8	13.5	24.4	3.2
MW-03	422	8-Mar-13	1303	0.517	0.19	8.6/24.1	4169	10.88	0.089	241	3310	105	4.11	0.03	106	999.4	421	1.2	1.53	6040	2.9	834	2.6	5.6	16.2	12.0	0.4
MW-03	524	3-Jun-13	1249	0.793	0.38	9.3/23.4	4280	12.92	0.127	239	3305	39	3.85	0.12	93	921.0	299	1.4	0.93	5850	0.3	910	1.6	5.0	14.0	7.8	0.9
MW-01	339	28-Nov-11	1191	4.482	2.41	8.9/24.5	7700	15.98	1.400	398	4195	274	0.61	2.878	110	745.5	184	N/A	3.08	7650	-5.5	2924	1.6	3.4	11.4	13.0	0.0
MW-01	353	9-Dec-11	966	4.826	2.76	8.8/21.8	7722	10.54	1.300	367	4358	264	0.93	1.412	114	568.0	178	N/A	3.07	7800	-2.2	6327	6.0	4.0	8.6	16.4	0.0
MW-01	310	10-Oct-12	1358	9.997	7.24	8.5/23.2	6038	70.72	1.175	443	4122	186	N/A	1.08	111	636.3	214	N/A	N/A	7860	5.3	4340	13.1	85.8	25.0	13.2	1.7
MW-01	767	7-Sep-13	1008	3.792	1.03	8.9/20.6	5228	0	0.002	521	3534	135	N/A	0.16	133	600.3	217	N/A	N/A	6170	3.2	2489	0.1	0.0	20.1	60.8	0.0
MW-04	325	18-Nov-11	1378	5.654	3.45	9.1/29.4	5698	241.4	1.874	411	3906	120	0.60	3.029	151	929.5	358	N/A	0.58	7040	-1.8	1900	34.4	78.1	4.4	16.6	0.0
MW-19	241	29-Apr-14	1594	4.413	2.9	7.3/21.5	479	11.9	0.485	286	425	49	N/A	0.1	37	74.6	259	N/A	N/A	1132	-1.4	306	3.4	9.6	0.2	86.3	5.5
MW-19	299	12-May-14	2093	9.308	8.62	9.6/23	407	20.4	1.141	589	683	23	N/A	0.1	71	314.7	226	N/A	N/A	1312	-4.1	240	5.2	29.3	0.7	66.8	1.6
MW-20	95	23-Mar-14	2132	8.963	8.28	8.9/20.9	2232	36.72	0.680	618	2030	246	N/A	0.01	201	579.1	280	N/A	N/A	2840	6.2	1684	10.5	105.7	26.9	0.0	0.0
MW-20	125	3-Apr-14	2376	12.07	12.1	8.8/19.9	2836	73.1	0.657	740	2139	334	N/A	0.01	272	613.6	128	N/A	N/A	3240	1.4	2212	15.3	154.8	34.7	3.5	0

h^{dt}: Total discharge enthalpy (kJ/kg)
p^{wh}: Well head pressure: p^{s} Sampling pressure
CBE ^{ic} (%) difference : $(\sum^{z}\text{cations} . {}^{m}\text{cations} - \sum^{z}\text{anions} . {}^{m}\text{anions}) / (\sum^{z}\text{cations} . {}^{m}\text{cations} + \sum^{z}\text{anions} . {}^{m}\text{anions}) * 100$
N/A: Analysis of the chemical component not available

3.2 Data quality

Prior to interpretation of the available data of the well discharge chemical analysis, the ubiquitous initial check of the quality based on the Charge Balance Error (CBE) was done by means of the following equation, which is based on electro-neutrality conditions:

$$CBE(\%) = \frac{\sum z_{cat}.m_{cat} - \sum z_{an}.m_{an}}{\sum z_{cat}.m_{cat} + \sum z_{an}.m_{an}} .100\% \quad (1)$$

where z_i is the charge of an ion, i, and m_i is the molal concentration of i (mol/kg). A CBE of the order of magnitude of 10% is invariably regarded as satisfactory (Arnórsson, 2000). Therefore, for the potentially complete data set of the aqueous component from the selected wells, a CBE within the permissible threshold was selected. For the water samples with a pH above 8.5, speciation of total inorganic carbon as HCO_3^- and silica as $H_3SiO_4^-$ was taken into account in the CBE calculations. The gaseous components' atmospheric contamination was used as a criterion for selecting suitable data for interpretation.

3.3 Concentration of the liquid and vapour components

Several studies on the subject of the chemistry of fluids collected from Menengai wells indicate that the fluids are generally of Na-HCO_3 type with a varying composition of the non-condensable gases (Malimo, 2013; ELC, 2013; GAB, 2013; Sekento, 2012; Kipng'ok, 2011). As already pointed out, this study will focus on evaluating the mineral-fluid interaction determined from modelled aquifer water from the chemical compositions of the liquid and vapour collected from 6 selected wells (MW-12, MW-03, MW-01, MW-04, MW-19, MW-20) in Menengai field (Table 1). The fluids are predominantly of Na-HCO_3 type with varying appreciable amounts of chloride content in excess of 500 mg/kg in all the aforementioned wells, except well MW-19 eventually discharged single phase steam only. In addition, SiO_2 also forms part of the major components dissolved in the liquid phase, which is strikingly high in wells MW-19 and MW-20 with concentrations above 500 mg/ kg.

The measured discharge enthalpy of the wells spanned between 966 to 2376 kJ/kg. The wells display a variable magnitude of excess enthalpy from intermediate to the high with MW-19 discharge showing dry steam characteristics. CO_2, H_2 and H_2S constitute the main volatile gas components that preferentially partitioned into the vapour phase sampled at sampling pressures of about 0.19 to 12.1 bar-g. The concentrations of these gases at the mentioned sampling pressures range from 240 to 6327, 0 to 243, 0.1 to 50.1 mmole/kg in the order of the highest to the lowest, respectively. The other major gases are N_2 and CH_4. Although the selected well MW-04 sample, identified herein as 325, displays a different trend from most of the other wells used in this study, other discharge samples from this well display a similar pattern as that of the other wells. The unavailability of certain components, indicated by (N/A), limited the evaluation fluid equilibrium with minerals that contain Fe and Al (in section 4.2).

3.4 Reservoir fluid composition

After taking into account the analytical quality of the data collected at varying pressures, the selected data set was modelled for aqueous speciation for the purposes of evaluating the reservoir fluid composition and mineral saturation state. The WATCH 2.4 program (Arnórsson et al., 1982; Bjarnason, 2010) was used for this exercise. Menengai wells intercepted a high temperature liquid dominated reservoir with the well discharges having a varying degree in the measured excess enthalpies (i.e. the enthalpy of the discharged fluids is higher than that of the enthalpy of steam saturated liquid at the aquifer temperature: $h^{dt} > h^{f,l}$). A twofold approach was used to reconstruct the aquifer fluid composition and the data was used in assessing the mineral fluid equilibria. Firstly, in Model 1, the reservoir was assumed to be liquid only, no heat transfer ($Q^e = 0$) from the rock to the

liquid, no immobilisation of liquid on the formation ($M^{e,l}= 0$) and no additional vapour inflow or loss of vapour ($M^{e,v}= 0$); therefore, no discharge enthalpy was taken into account in the WATCH program since boiling is adiabatic (Arnórsson et al., 2007). In addition, the well discharge enthalpy is the same as that of the parent aquifer fluid.

In Model 2, the system was considered to be closed and that the excess well discharge enthalpy was accounted for by two-phase liquid and vapour reservoir fluid, the cause of the excess enthalpy being heat transfer ($Q^e \neq 0$) to fluids. It is for this reason that the processes leading to the excess discharge enthalpy will also be evaluated, based on the presented data.

The reservoir fluid composition was calculated with the aid of the WATCH 2.4 program (Arnórsson et al., 1982; Bjarnason, 2010). For conservation of mass we have:

$$m_i^{f,t} = m_i^{d,t} = m_i^{d,v}\mathrm{X}^{d,v} + m_i^{d,l}(1 - \mathrm{X}^{d,v}) \quad (2)$$

where $m^{f,t}$ $m^{d,t}$, $m^{d,v}$, and $m^{d,l}$ stand for molal concentration of the dissolved component *i* for the parent liquid, total discharge, in vapour and in liquid, respectively. $\mathrm{X}^{d,v}$ is the vapour mass fraction of the well discharge, hence, the liquid mass fraction becomes $(1\text{-}X^{d,v})$. For conservation of enthalpy we have:

$$h^{f,t} = h^{d,t} = h^{d,v}\mathrm{X}^{d,v} + h^{d,l}(1 - \mathrm{X}^{d,v}) \quad (3)$$

and

$$\mathrm{X}^{d,v} = \frac{h^{d,t} - h^{d,l}}{h^{d,v} + h^{d,l}} \quad (4)$$

where $h^{d,t}$, $h^{d,v}$, and h^{dl} designate the total discharge enthalpy, enthalpy of saturated steam and enthalpy of saturated liquid, respectively.

For Model 1, the vapour fraction in the reservoir is considered to be zero, and the reservoir enthalpy is calculated based on the reservoir temperature, assuming liquid only. For Model 2, the reservoir is considered to include a vapour fraction, i.e. the mass and enthalpy equations are solved using the measured discharge enthalpy as the total enthalpy of the system along with the reservoir temperature. The quartz geothermometer temperature was adopted, assuming that the aquifer fluids are in equilibrium with quartz.

3.5 Aqueous speciation and mineral saturation

The aqueous speciation distribution was calculated using the WATCH 2.4 program (Arnórsson et al., 1982; Bjarnason, 2010). From those, the mineral saturation state was calculated from:

$$SI = \log(Q/K) \quad (5)$$

where K is the equilibrium solubility constant and Q is the activity product (Q) given by:

$$Q = \prod_i a_i^{v_i} \quad (6)$$

and a_i represents the respective aqueous species activities raised to the power of its stoichiometric coefficient v_i, which is negative for reactants and positive for products.

This study focused on assessing the saturation state of selected hydrothermal minerals including end-members of solid solutions. The minerals include: anhydrite, andradite-grossular, calcite, clinozoisite–epidote, fluorite, hematite, magnetite, Al–prehnite, pyrite, pyrrhotite, wollastonite, albite, K-feldspar, anorthite, paragonite and muscovite. A summary of the alteration mineralogy in Menengai geothermal system is presented in Section 2.3 of this report.

The equilibrium constants for dissolution reactions involving various individual minerals used in this study are presented in Table 2, adopted from the work of Karingithi et al. (2010) and Arnórsson, and Stefánsson (1999). The aforementioned authors took into account the standard thermodynamic properties (ΔG_f^O, S^O, V^O, C_P^O) of the various mineral dissolution reactions and derived them from a wide range of sources. Feldspar solubility constants used in this study are those given by Arnórsson, and Stefánsson (1999) and are valid from 0 to 350 at saturated water and vapour pressure. Equations describing the temperature dependence of the solubility constants of reactions for end member feldspars are also given in Table 2, taking into account the acid calorimetry results for the microcline and sanidine (K- feldspars) solubility constants. The saturation state of other minerals, such as anhydrite and micas, were also evaluated. Thermodynamic data of anhydrite solubility constants were retrieved from Gudmundsson and Arnórsson (2005), based on an experiment which took into consideration the Na-SO_4 iron pairing, whereas the mica functions were based on the Na-K geothermometry equation of Fournier (1991).

The mineral-gas reactions that could potentially control the concentrations of CO_2, H_2S, and H_2 in the aquifer liquid and temperature equations for their equilibrium constants are listed in Table 3, adopted from the work of Karingithi et al. (2010) and Arnórsson et al. (2010) who retrieved thermodynamic data of various minerals from a wide range of sources, as already pointed out. The equations in Table 3 assume a unit activity of all minerals and liquid water ($H_2O_{(l)}$). However, as for the equilibrium curves shown and discussed in chapter 5.5, their respective equations were slightly modified to take into account the activities of end-members of minerals that form solid solutions (epidote, garnet and prehnite).

Then, considering reaction 3 in Table 3 we have:

$$\log \mathrm{K} = \frac{2}{3}\log(a_{epi}) + \log(a_{H_2S}) - \frac{1}{3}\log(a_{pyr}) - \frac{1}{3}\log(a_{pyrr}) - \frac{2}{3}\log(a_{pre}) - \log(a_{H_2O}) \quad (7)$$

Taking the activities of pyrite (pyr), pyrrhotite (pyrr) and water to be equal to unity, but those of epidote and prehnite in the epidote and prehnite solid solutions to be both 0.8, and in order to determine the equilibrium concentration of aqueous (H_2S) in the initial aquifer, Equation 12 is reduced to:

$$\log(a_{H_2S}) = \log \mathrm{K} + \frac{2}{3}\log(a_{pre}) - \frac{2}{3}\log(a_{epi}) \quad (8)$$

At the time of this present study, there was no data available on the mineral activity from Menengai geothermal system, therefore, the mineral compositions were assumed to be the same as those of the Olkaria system, taken from Karingithi et al. (2010) and Arnórsson et al. (2010). For end-member epidote [$(Ca_2Al_2FeSi_3O_{12}(OH)]$, the activity was taken to be 0.8, for end-member prehnite [$(Ca_2Al_2Si_3O10(OH)_2$] the activity was taken to be 0.8, assuming Al-prehnite, and activity on the order of 0.3 and 0.2 was chosen for grossular and clinozoisite, respectively.

TABLE 2: Temperature equations for equilibrium constants for individual mineral dissolution reactions; the logK is valid in the range 0 to 350°C and at saturated water vapour pressure; unit activity was selected for all minerals and liquid water (Karingithi et al., 2010; Arnórsson, and Stefánsson, 2009; Gudmundsson and Arnórsson, 2005)

	Mineral	Abbreviation	Reaction	Log (K) function
1	Andradite	and	$and + 4H^+ + 8H_2O_{(l)} = 3Ca^{+2} + 2Fe(OH)_4^- + 3H_4SiO_4^o$	$+940.225 - 15419.3/T + 0.58092.T - 0.0002971.T^2 - 421.727.logT$
2	Calcite	cal	$cal + 2H^+ = Ca^{+2} + H_2O_{(l)} + CO_{2(aq)}$	$-68.271 + 4385.24/T - 0.007525.T + 28.856.logT$
3	Clinozoisite	czo	$czo + 12H_2O_{(l)} = 2Ca^{+2} + 3Al(OH)_4^- + 3H_4SiO_4^o + OH^-$	$+36.052 - 6854.78/T + 0.13236.T - 0.00013749.T^2 - 33.508.logT$
4	Epidote	epi	$epi + 12H_2O_{(l)} = 2Ca^{+2} + Fe(OH)_4^- + 2Al(OH)_4^- + 3H_4SiO_4^o + OH^-$	$+893.547 - 27077.4/T + 0.54124.T - 0.0003022.T^2 - 398.380.logT$
5	Flourite	flu	$flu = Ca^{+2} + 2F^-$	$+64.54 - 4318/T - 25.74.logT$
6	Grossular	gro	$gro + 4H^+ + 8H_2O_{(l)} = 3Ca^{+2} + 2Al(OH)_4^- + 3H_4SiO_4^o$	$-517.662 + 17623.7/T - 0.14343.T + 203.808.logT$
7	Magnetite	mag	$mag + 4H_2O_{(l)} = 3Ca^{+2} + 2Fe(OH)_4^- + Fe^{+2}$	$+949.951 - 24258.2/T + 0.51474.T - 0.0002402.T^2 - 417.136.logT$
8	Prehnite	pre	$pre + 10H_2O_{(l)} = 2Ca^{+2} + 2Al(OH)_4^- + 3H_4SiO_4^o + OH^-$	$+833.950 - 25642.8/T + 0.5035.T - 0.0002941.T^2 - 369.297.logT$
9	Pyrite	pyr	$pyr + 2H^+ + H_{2(aq)} = 2H_2S_{(aq)} + Fe^{+2}$	$-1.397 - 461.30/T - 0.0009128.T + 1.626.logT$
10	Pyrrhotite	pyrr	$pyrr + 2H^+ = 2H_2S_{(aq)} + Fe^{+2}$	$-3.043 + 1579.06/T + 0.0001987.T + 0.120.logT$
11	Quartz	qtz	$qtz + 2H_2O_{(l)} = H_4Si_4^o$	$-34.188 + 197.47/T - 5.851 \times 10^{-6}.T^2 + 12.245.logT$
12	Wollastonite	wol	$wol + 2H^+ + H_2O_{(l)} = Ca^{+2} + H_4Si_4^o$	$-127.096 + 8151.38/T - 0.2981.T + 49.282.logT$
13	Anhydrite	anh	$anh + 2H^+ = Ca^{+2} + SO_4^{-2}$	$+78.414 - 3247.2/T - 9.03 \times 10^{-7}T^2 - 28.723.logT$
	Felspars			
14	Low Albite	alb^l	$NaAlSi_3O_8 + 8H_2O_{(l)} = Na^+ + Al(OH)_4^- + 3H_4SiO_4^o$	$-96.267 + 305542/T^2 - 3985.50/T - 28.588 \times 10^{-6}.T^2 - 35.7790.logT$
15	High Albite	alb^h	$NaAlSi_3O_8 + 8H_2O_{(l)} = Na^+ + Al(OH)_4^- + 3H_4SiO_4^o$	$-97.275 + 306065/T^2 - 3313.51/T - 28.622 \times 10^{-6}.T^2 - 35.851.logT$
16	Microline	mic	$KAlSi_3O_8 + 8H_2O_{(l)} = K^+ + Al(OH)_4^- + 3H_4SiO_4^o$	$-78.594 + 311970/T^2 - 6094.13/T - 27.766 \times 10^{-6}.T^2 - 30.308.logT$
17	Sanidine	san	$KAlSi_3O_8 + 8H_2O_{(l)} = K^+ + Al(OH)_4^- + 3H_4SiO_4^o$	$-77.837 + 316431/T^2 - 5744.85/T - 27.712 \times 10^{-6}.T^2 - 29.738.logT$
18	Anorthite	ano	$CaAl_2Si_3O_8 + 8H_2O_{(l)} = Ca^{+2} + 2Al(OH)_4^- + 3H_4SiO_4^o$	$-88.591 + 326546/T^2 - 2720.61/T - 40.100 \times 10^{-6}.T^2 - 31.168.logT$

Thermodynamic data used in Equations 1-12 was retrieved from a wide range of sources as elucidated by Karingithi et al. (2010) while that of anhydrite (Equation 13) from Gudmundsson and Arnórsson (2005)
The solubility of end-member feldspars (Equations 14-18) were adopted from Arnórsson and Stefánsson (1999,2000).

TABLE 3: LogK-temperature equations for mineral pair and mineral assemblage reactions that may control the gas concentrations in solution; the equations are valid in the range 0–350°C at vapour saturation pressures; unit activity was selected for all minerals and liquid water

		Reaction	Log (K) function
1	CO_2	$czo + \text{cal} + \frac{3}{2}\text{qtz} + H_2O_{(l)} = \frac{3}{2}\text{pre} + CO_{2(aq)}$	$-0.890 + 7251.5/T^2 - 1710.6/T + 0.004188T + 0.000002683T^2 - 0.0624logT$
2	CO_2	$\frac{2}{5}czo + \text{cal} + \frac{3}{5}\text{qtz} + = \frac{3}{5}\text{gro} + \frac{1}{5}H_2O_{(l)} + CO_{2(aq)}$	$-1.449 - 40536/T^2 - 2135.9/T + 0.0065639T + 0.000002725T^2 - 0.193logT$
3	H_2S	$\frac{1}{3}pyr + \frac{1}{3}\text{pyrr} + \frac{2}{3}\text{pre} + \frac{2}{3}H_2O_{(l)} = \frac{2}{3}\text{epi} + H_2S_{(aq)}$	$+13.608 + 592324/T^2 - 9346.7/T - 0.043552T + 0.000029164T^2 + 5.139logT$
4	H_2S	$\frac{2}{3}gro + \frac{1}{3}\text{pyr} + \frac{1}{3}\text{pyrr} + \frac{2}{3}\text{qtz} + \frac{4}{3}H_2O_{(l)} = \frac{2}{3}\text{epi} + \frac{2}{3}\text{wol} + H_2S_{(aq)}$	$+13.659 + 555082/T^2 - 9256.6/T - 0.043608T + 0.000028613T^2 + 5.148logT$
5	H_2S	$2gro + \frac{1}{4}\text{pyr} + \frac{1}{2}\text{mag} + 2\text{qtz} + 2H_2O_{(l)} = 2\text{epi} + 2\text{wol} + H_2S_{(aq)}$	$-0.836 - 216659/T^2 - 2847.3/T + 0.008524T - 0.000002366T^2 + 0.152logT$
6	H_2S	$\frac{1}{4}\text{pyr} + \frac{1}{2}\text{pyrr} + H_2O_{(l)} = \frac{1}{4}\text{mag} + H_2S_{(aq)}$	$+13.589 + 590215/T^2 - 9024.5/T - 0.044882T + 0.000029780T^2 + 5.068logT$
7	H_2	$\frac{4}{3}\text{pyrr} + \frac{2}{3}\text{pre} + \frac{2}{3}H_2O_{(l)} = \frac{2}{3}\text{epi} + \frac{2}{3}\text{pyr} + H_{2(aq)}$	$-1.640 - 124524/T^2 - 777.19/T - 0.0005501T + 0.000007756T^2 - 0.565logT$
8	H_2	$\frac{2}{3}\text{gro} + \frac{4}{3}\text{pyrr} + \frac{2}{3}\text{qtz} + \frac{4}{3}H_2O_{(l)} = \frac{2}{3}\text{epi} + \frac{2}{3}\text{wol} + \frac{2}{3}\text{pyr} + H_{2(aq)}$	$-1.544 - 151109/T^2 - 752.389/T - 0.0005868T + 0.000007080T^2 - 0.532logT$
9	H_2	$6\text{gro} + 2\text{mag} + 6\text{qtz} + 4H_2O_{(l)} = 6\text{epi} + 6\text{wol} + + H_{2(aq)}$	$+1.444 - 273812/T^2 - 3962.1/T + 0.002401T + 0.000001304T^2 + 0.979logT$
10	H_2	$\frac{2}{3}\text{pyrr} + H_2O_{(l)} = \frac{3}{4}\text{pyr} + \frac{1}{4}\text{mag} + H_{2(aq)}$	$-1.654 - 95456.8/T^2 - 621.84/T - 0.001257T + 0.000007569T^2 - 0.600logT$
The wide range of sources of thermodynamic data used to obtain the temperature equations is outlined by Karingithi et al. (2010) and Arnórsson et al. (2010)			

4. RESERVOIR FLUID COMPOSITION AND TEMPERATURES

4.1 Reservoir fluid chemical composition

The reservoir fluid compositions calculated, assuming liquid only reservoirs (Model 1) and two-phase reservoirs (Model 2), are given in Tables 4 and 5, respectively.

TABLE 4: Chemical composition of initial aquifer fluid assuming liquid only reservoir (Model 1)

Well No.		MW12	MW12	MW12	MW03	MW03	MW03	MW01	MW01	MW01	MW01	MW04	MW19	MW19	MW20	MW20
Sample No.		414	438	474	323	422	524	339	353	310	767	325	241	299	95	125
$h^{d,l}$ (kJ/kg)		876	969	1040	777	768	767	932	912	992	1011	946	840	1099	1121	1219
$T^{f,qtz}$		205.3	225.5	240.4	183.1	181.1	180.8	217.5	213.2	230.4	234.4	220.5	197.3	252.7	257.3	276.5
pH		6.5	6.6	6.7	6.7	6.7	6.8	6.7	6.3	6.7	6.6	6.9	6.5	7.2	6.8	7.0
Dissolved solids (mg/kg)	B	0.3	0.2	0.3	0.3	0.1	0.1	1.2	1.1	1.0	0.0	1.6	0.4	0.9	0.6	0.5
	SiO_2	283	363	429	211	206	206	333	313	385	402	348	254	488	504	589
	Na	2181	2874	2896	2524	2825	2848	3510	3713	3586	2725	3306	377	567	1656	1702
	K	86	56	94	85	90	34	229	225	162	104	102	44	19	201	266
	Mg	0.25	2.9	0.28	2.68	3.5	3.3	0.510	0.79	0	0	0.508	0	0	0	0
	Ca	0.22	0.02	0.38	0.23	0.03	0.1	2.41	1.2	0.94	0.12	2.56	0.09	0.08	0.01	0.01
	F	60	62	52	83	90	80	92	97	96	102	128	33	59	164	217
	Cl	545	582	737	843	853	794	624	484	553	463	787	67	261	472	489
	SO_4	291	358	227	355	421	299	184	178	214	217	358	259	226	280	128
	Al	0.33	0.22	0.4	0.73	1.02	1.21	N/A	N/A	N/A	N/A	N/A	N/A	N/A	N/A	N/A
	Fe	0.01	0.56	0.23	0.67	1.31	0.80	2.58	2.62	N/A	N/A	0.49	N/A	N/A	N/A	N/A
	TDS	4527	4940	4725	5313	5156	5040	6400	6645	6839	4758	5958	2007	1088	2317	2578
Dissolved gases (mg/kg)	CO_2	16386	25508	27407	9862	8932	9230	27467	47806	30068	29102	17673	1933	2137	15467	22137
	H_2S	178	241	341	28	22	19	22	39	120	0.8	384	24	47	66	165
	H_2	31.0	51.7	44.1	1.8	1.8	1.4	1.0	1.2	22.5	0.0	24.2	2.3	10.0	39.4	63.9
	CH_4	19.3	39.9	35.3	31.3	38.0	31.1	29.9	20.4	52.1	73.8	10.9	0.4	1.9	79.5	113.7
	N_2	51.0	39.0	21.1	97.1	49.2	31.0	59.5	66.4	48.0	391.0	73.2	269.7	319.7	0	22.9
	O_2	0	0	0	13.9	0	4.4	0	0	7.1	0	0	19.7	8.7	0	0

$h^{d,l}$: Liquid enthalpy (kJ/kg) at aquifer quartz temperature

$T^{f,qtz}$: Aquifer temperature based on quartz geothermometer temperature

The chemical composition, with respect to major non-volatile elements, is relatively unaffected by the selection of the model when calculating the reservoir fluid composition from the data on water and vapour collected from the well discharges at the surface. The exception to this is when the well discharges approach dry steam (Figure 2). The concentrations of non-volatiles, including SiO_2, Na, K, Mg, Ca, F,Cl, SO_4, Al and Fe, were, however, systematically lower when assuming a liquid-only reservoir compared to two-phase reservoirs.

When assuming reservoir vapour to be present, the concentration of the volatiles in the reservoir water phase is significantly lower than when assuming a single liquid reservoir. The reason for the former is that the volatiles, including CO_2, H_2S, H_2, CH_4, N_2 and O_2, tend to partition into the vapour phase where CH_4 and H_2 somewhat completely enter a steam phase, with little amounts in the liquid phase, whereas CO_2 and H_2S are distributed between the two phases. Also, there is some variability in the elemental concentrations between wells. The depletion of H_2 in the reservoir fluids of some samples from wells MW-03 and MW-01 could be due to boiling processes. It is worth noting that the reconstructed reservoir fluid chemistry of well MW-19 sample 241 seemingly does not agree with that of the other wells and could have been subdued by a possible discharge that was dominated by residual drilling fluid prior to its eventual single-phase steam-only discharge.

TABLE 5: Chemical composition of initial aquifer fluid assuming liquid and vapour reservoir (Model 2)

Well No.		MW12	MW12	MW12	MW03	MW03	MW03	MW01	MW01	MW01	MW01	MW04	MW19	MW19	MW20	MW20
Sample No.		414	438	474	323	422	524	339	353	310	767	325	241	299	95	125
$h^{d,t}$ (kJ/kg)		1600	1492	1580	1267	1303	1249	1191	966	1358	1011	1378	1594	1293	2132	2376
$T^{f,qtz}$		194	204	221	130	125	121	183	207	210	234	176	184	240	240	260
pH		7.7	8.0	7.9	8.6	8.7	8.8	8.2	7.4	7.9	6.6	8.3	8.0	8.1	8.0	8.0
Dissolved solids (mg/kg)	B	0.31	0.18	0.28	0.38	0.08	0.12	1.26	1.12	1.08	0.00	1.77	0.45	0.94	0.57	0.54
	SiO_2	290	378	445	235	230	233	359	317	404	402	384	258	504	515	608
	Na	2232	2991	3009	2810	3159	3220	3788	3764	3755	2725	3648	383	585	1693	1758
	K	88	58	98	94	100	38	247	228	169	104	112	44	20	205	274
	Mg	0.26	3.01	0.30	2.98	3.92	3.75	0.55	0.80	0.00	0.00	0.56	0.00	0.00	0.00	0.00
	Ca	0.22	0.03	0.4	0.26	0.03	0.12	2.6	1.22	0.98	0.12	2.83	0.09	0.09	0.01	0.01
	F	61	64	54	92	101	90	99	98	101	102	141	33	61	168	224
	Cl	557	606	766	938	953	897	674	491	579	463	869	68	270	483	505
	SO_4	279	308	191	338	402	291	166	154	195	167	334	234	194	234	105
	Al	0.34	0.23	0.41	0.81	1.15	1.36	0	0	0	0	0	0	0	0	0
	Fe	0.01	0.58	0.24	0.74	1.46	0.91	2.78	2.65	0	0	0.54	0	0	0	0
	TDS	4633	5142	4909	5916	5765	5700	6907	6738	7160	4758	6575	2038	1124	2369	2662
Dissolved gases (mg/kg)	CO_2	3710	4536	4489	3961	3697	4415	7619	10383	6316	29102	5754	348	559	2356	3365
	H_2S	189	206	265	25	24	17	18	27	95	1	385	18	43	79	128
	H_2	0.18	0.17	0.23	0	0	0	0	0.02	0.12	0	0.04	0.01	0.14	0.3	0.76
	CH_4	0.11	0.14	0.19	0.01	0.01	0.01	0.06	0.29	0.29	73.79	0.02	0	0.03	0.63	1.39
	N_2	0.18	0.08	0.07	0.02	0.01	0	0.07	0.58	0.17	391.04	0.06	0.42	3.23	0	0.21
	O_2	0	0	0	0	0	0	0	0	0.04	0	0	0.05	0.12	0	0
Vapour phase (mg/kg)	CO_2	221860	160304	162727	44897	40255	41595	174121	1045559	241781	0	94849	15524	18309	81343	102886
	H_2S	1635	964	1213	74	71	48	61	419	474	0	990	122	177	346	530
	H_2	523	384	305	13	13	11	8	32	221	0	180	23	108	236	332
	CH_4	327	296	244	237	281	236	251	553	512	0	81	4	21	475	590
	N_2	863	290	146	736	364	235	500	1804	472	0	545	2754	3456	0	119
	O_2	0	0	0	105	0	34	0	0	69	0	0	201	94	0	0

$h^{d,t}$: Total measured discharge enthalpy (kJ/kg)

$T^{f,qtz}$: Aquifer temperature based on quartz geothermometer temperature

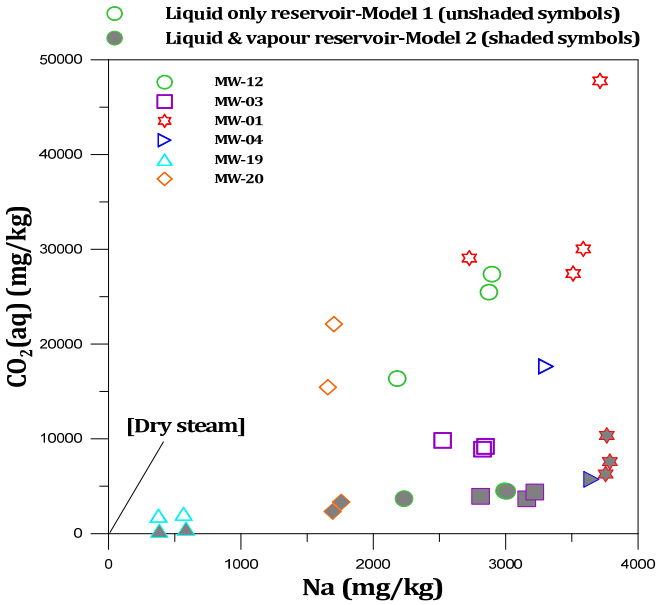

FIGURE 2: Correlation of the concentration of major non-volatile and major volatile components in Menengai aquifer waters

In addition, in both models the boron concentration in reservoir liquids from wells MW-01, MW-04 and MW-19 is generally higher than in the other wells. This could be due to the occurrence of boiling at different depths, determining the enrichment in boric acid in the steam-heated overlying aquifer waters (ELC, 2013). On the other hand, fluoride concentration is distinctly high in Menengai reservoir fluids and ranges from 32 to 217 mg/kg, with well MW-20 having an excess of 150 mg/kg. The fluoride content in the fluids was compared with that of Olkaria 15 and 310, presented in Arnórsson et al. (2010); this high concentration could be reminiscent of the deep fluids of the Kenya's Rift.

4.2 Aquifer temperature

Quartz, Na/K and H_2S were used to estimate the reservoir temperature, using both Models 1 and 2 (Figure 3). The Na/K gives the lowest value of the estimated temperature, although the result is the same for both models as it is based on a ratio (Table 1 in Appendix I). H_2S gives the highest temperature when assuming a liquid-only reservoir, and with a lower temperature when assuming a reservoir with vapour present; this is due to the low dissolved volatile concentrations in the latter case, as the H_2S tends to partition into the vapour phase.

Generally, the results for both models indicate an outright discrepancy in the geothermometer temperatures in most of the wells except for a near conformity seen in well MW-20 and sample 241 of well MW-19 for Na/K against quartz. The conformity in wells MW-19 and MW-20 could substantiate that the samples might have been diluted by condensed steam since their high discharge enthalpy approaches that of dry steam. Samples from well MW-20 and sample 339 from well MW-01 show good conformity between the H_2S and quartz geothermometer temperatures, assuming a liquid only reservoir due to high dissolved H_2S in the aquifer water. The discrepancy in other well samples could be due to the mixing of fluids from different aquifers of significantly varying temperatures, as discussed by Arnórsson (2000). Relatively high sulphate content in the wells showing the non-conformity may confirm the lower temperatures (<200°C), whereas relatively low sulphate content, i.e. in well MW-20, gives high temperatures.

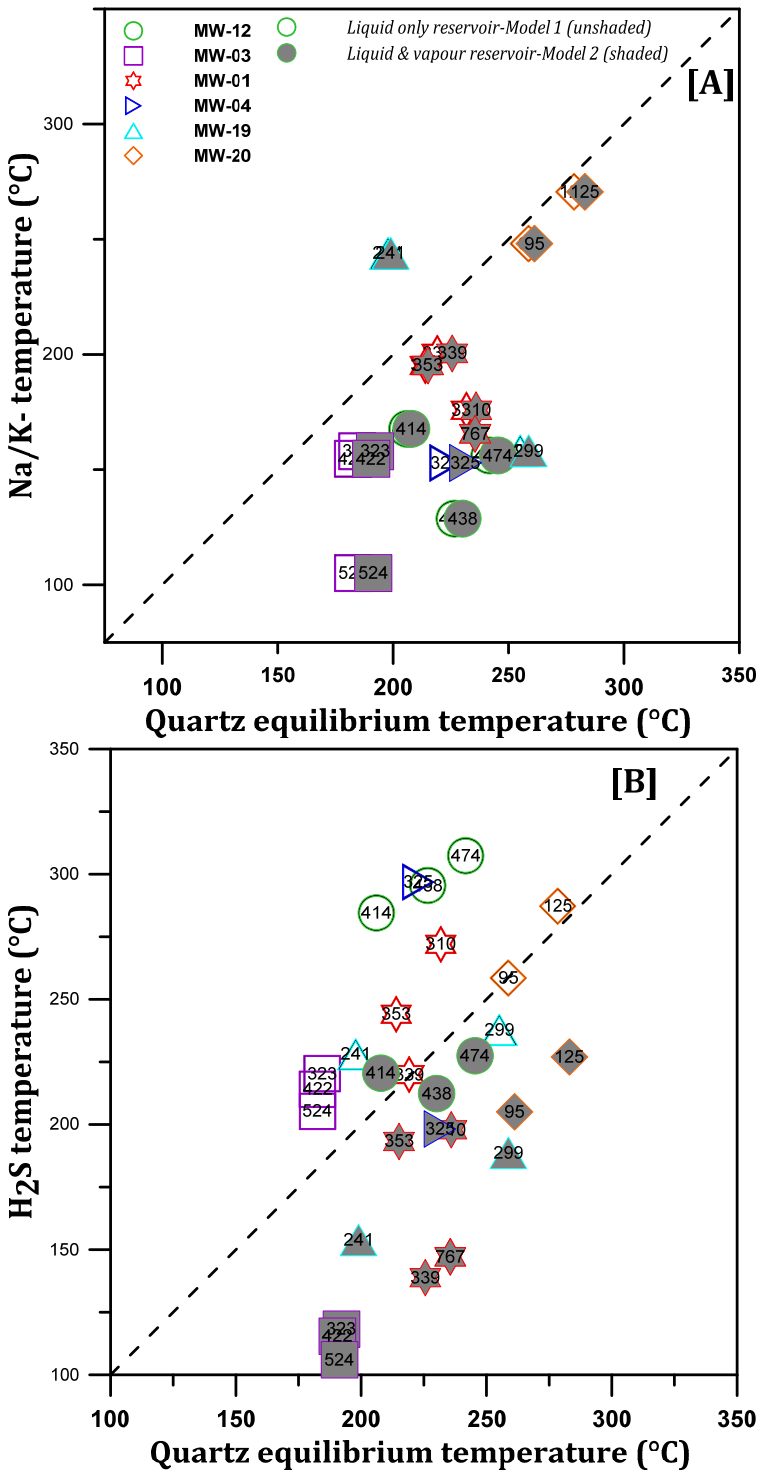

FIGURE 3: Relationship between geothermometer temperatures in Menengai wells, based on Models 1 and 2; A) Quartz function of Fournier and Potter (1982), Na/K (Giggenbach, 1988), B) H_2S (equilibrium with the assemblage of magnetite + pyrite + pyrrhotite was assumed (Equation 6 - Table 3))

GAB (2013) pointed out that, at depths below 2000 m, the wells penetrated a soft layer (magma) and encountered super-heated steam with measured temperatures of almost 400°C and pressure that was

well below critical pressure (Pc), 160 bars as compared Pc = 221 bars. In this typical scenario, most wells encountered one or two aquifers above the zone of super-heated steam, one at ~1000-1300 m depth and the other at 1500-1800 m. The upper aquifer seems to be sub-boiling, at ~200°C. The deeper liquid water aquifer is hotter, likely around 250°C. Therefore, the geothermometer temperatures may represent mixed reservoir fluid composition and may not represent a given fluid equilibrated at a given temperature.

5. FLUID MINERAL INTERACTION

Water-rock interaction is conventionally viewed as an irreversible acid-base titration where the water with it dissolved gases acts as the acid while the aggregate of the rock forming minerals act as the base to form stable or metastable secondary minerals. Equilibrium between the hydrothermal solutions and individual minerals was evaluated in this study. This included common hydrothermal minerals observed in the Menengai field and other volatile mineral buffers that potentially control the concentration of CO_2, H_2S and H_2 in most volcanic geothermal systems.

5.1 Calcite, wollastonite, fluorite and anhydrite

The saturation states of calcite, wollastonite, fluorite and anhydrite in the initial aquifer waters, calculated for selected wells in the Menengai geothermal system, are presented in Figure 4. Generally, the log Q values of calcite (Figure 4A) display a remarkable departure from the equilibrium constant curve for virtually all the samples computed by Model 1, except for sample 325 from well MW-04 which is slightly over saturated (0.2 SI units), possibly due to its high measured pH value (Table 1). The departure is in the range of 0.2 to -2.56 SI units with a mean of –1.44 SI units, reflecting under-saturation of the initial aquifer fluids with respect to calcite.

Alternatively, Model 2 yields a considerable scatter with a mean deviation of -0.3 SI units, for instance five under saturated, two near equilibrium and ten samples under-saturated. It is also worth noting that the computed pH value for Model 2 is 8.8 on average, which is higher than that of Model 1 (on average 6.7 pH units), affecting the calculated activities of aqueous $CO_{2(aq)}$. Therefore, the pH value obtained for the parent liquid water affects the saturation state of calcite and other minerals whose solubility is pH dependent. Calcite appears in almost the entire stratigraphic column of most Menengai wells.

Calcite under-saturation could be attributed to the high content of dissolved CO_2 which buffers the aquifer pH and consequently affects the kinetics of the solubility of wollastonite; other silicate minerals will be discussed below. Karingithi et al. (2010) also pointed out that the saturation state of wollastonite, fluorite and calcite are intimately dependent on analytical errors and thermodynamics. Therefore, analytical uncertainties resulting from a possible error during the measurement of the pH may be another possible cause for under-saturation. Wollastonite (Figure 4B), fluorite (4C) and anhydrite (4D) are strongly under-saturated in the aquifer waters based on both Models 1 and 2. The removal of Ca from the solution, in order to precipitate calcite from the flashed water and ultimately lead to low Ca in the discharged water, could also substantiate the under-saturation of wollastonite, fluorite and anhydrite. Therefore, the under-saturation of these minerals could also be a function of the kinetics of their dissolution in relation to that of calcite precipitation. Anhydrite is a common hydrothermal mineral found in the lower portions of the chlorite-epidote zone (Freeman et al., 2010). Its stability is considered to be linked with that of epidote (Gudmundsson and Arnórsson, 2005). The observed under-saturation of epidote could also lead to the under-saturation of anhydrite.

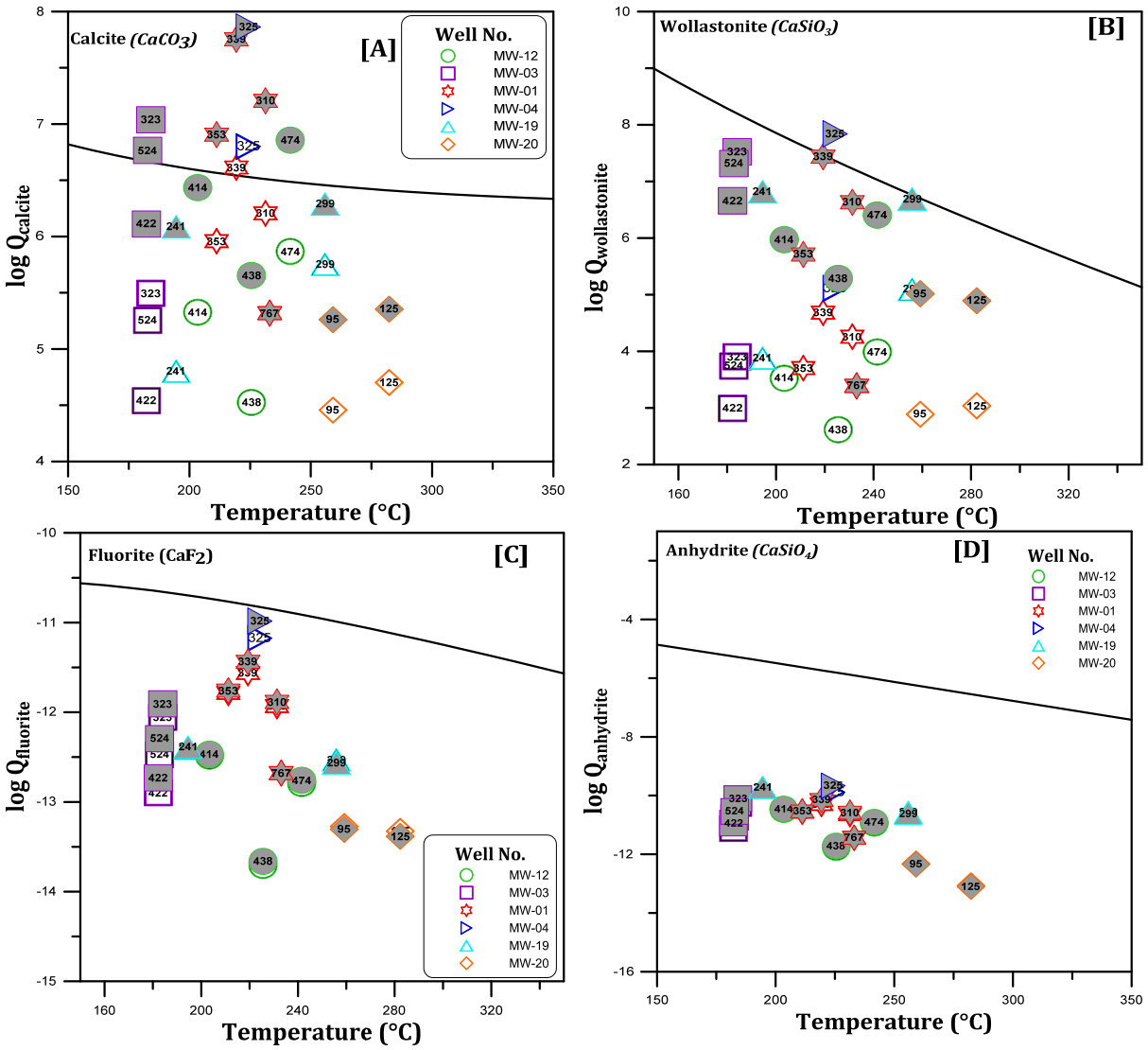

FIGURE 4: Saturation state of Menengai aquifer waters with respect to calcite (A), wollastonite (B), fluorite (C) and anhydrite (D); Model 1: unshaded symbols, Model 2: shaded

5.2 Andradite–grossular, clinozoisite–epidote, and prehnite

Menengai aquifer waters show under-saturation with respect to grossular (Figure 5A), clinozoisite (Figure 5B), and prehnite (Figure 6A) in both models. The logQ values of andradite, based on Model 1, have remarkably deviated from the equilibrium curve (under-saturated) with a mean SI of -5.3, although sample 353 from well MW-01 is close to equilibrium. Alternatively, when assuming a liquid and vapour reservoir, the andradite SI values seem to reflect oversaturation with an average of 3.6 SI units; but two samples, 414 and 438, from well MW-12, are under-saturated and are somewhat close to the equilibrium curve.

The state of epidote saturation in Menengai waters, based on Model 1, indicates a deviation corresponding to indistinct SI values in the range of -1.37 to 0.97 with some being oversaturated (samples 474 and 323 from wells MW-12 and MW-03, respectively) whereas the rest of the samples are under-saturated. On the other hand, upon assuming a liquid and vapour reservoir (Model 2), epidote is oversaturated (1.56 SI units on average) in virtually all the samples.

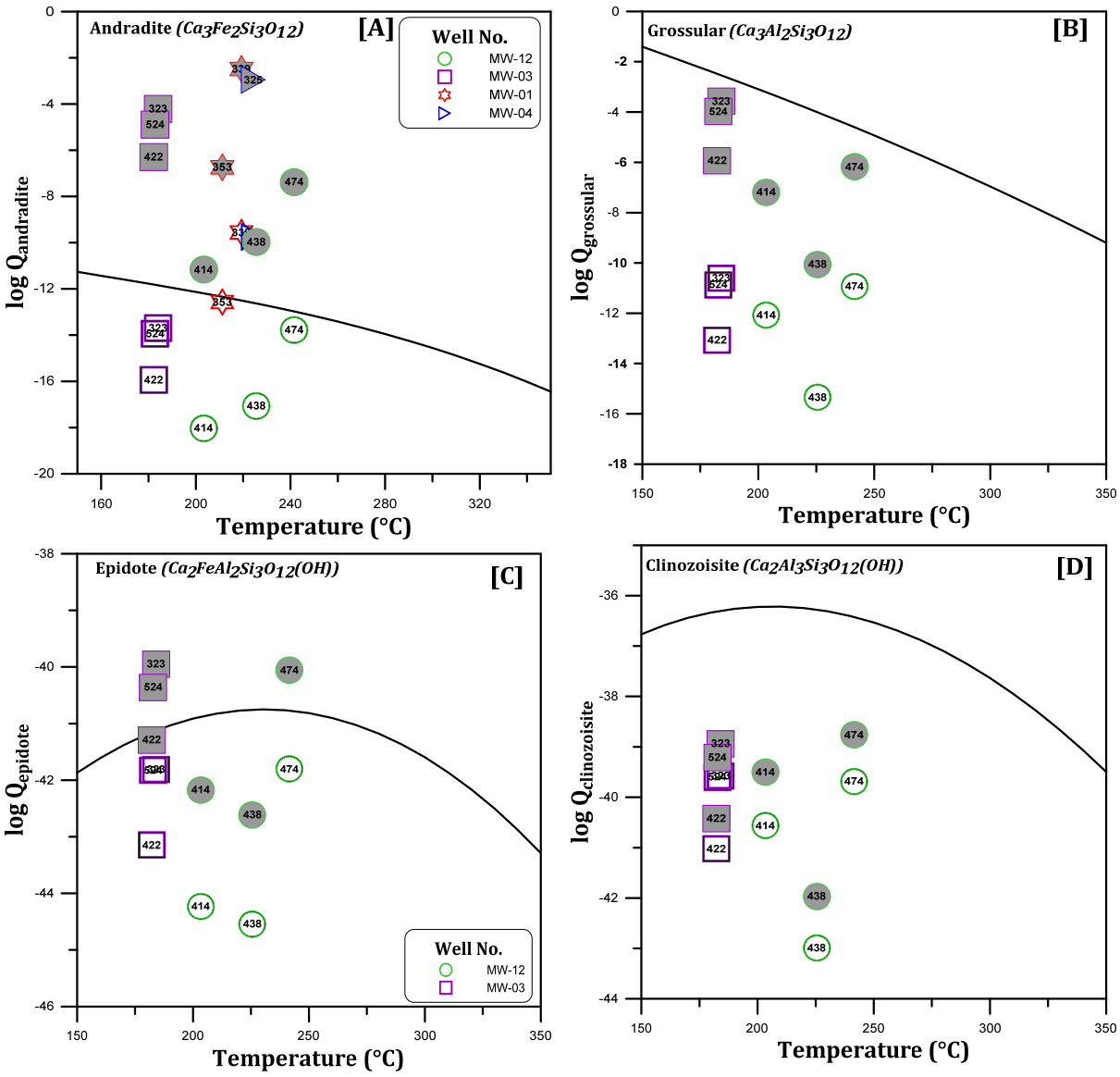

FIGURE 5: Saturation state of Menengai aquifer waters with respect to andradite (A), grossular (B), epidote (C) and clinozoisite (D); Model 1: unshaded symbols; Model 2: shaded

The saturation state of these minerals can be attributed to the following: The solubility of the Ca-alumino-silicate minerals, particularly the garnet minerals (grossular and andradite), is strongly dependent on the pH as per their stoichiometric reactions. Gudmundsson and Arnórsson (2005) concluded that since garnet invariably forms under contact metamorphism, its oversaturation in the Krafla aquifer fluids owes its existence to a temporary development due to magmatic intrusions in the reservoir. Albeit not observed in the rock cuttings, this reason could also explain oversaturation of andradite-garnet in the Menengai aquifer waters when computed with Model 2, while taking into account the intercepted intermittent magmatic intrusions.

The scatter from equilibrium displayed by the OH bearing silicates could also be due to the stoichiometry of the respective minerals, the OH-bearing silicates (epidote, clinozoisite and prehnite) having the largest number of cations per OH. For minerals (andradite and epidote) which contain Fe (III), over- estimation of the $Fe(OH)_4^-$ activity is considered to be the possible cause for the positive SI values recorded, as per the study of ferrous and ferric hydrolysis constants above 200°C by Arnórsson et al. (2002) and underpinned by Karingithi et al. (2010).

5.3 Magnetite, pyrite, and pyrrhotite

Menengai initial aquifer waters are systematically oversaturated with respect to magnetite (9 SI units on average in both models), pyrite and partly with pyrrhotite which has a few samples that are under-saturated when computed with respect to the two models (Figure 6).

The generally observed oversaturation of these minerals in Menengai aquifer waters compares with that of the initial aquifer waters of Námafjall (Gudmundsson and Arnórsson, 2005) and that of Olkaria (Karingithi et al, 2010). It, therefore, follows that the deviation of logQ values of these Fe (II) bearing minerals is largely due to the variations in the calculated activities (Gudmundsson and Arnórsson, 2005; Karingithi et al., 2010). The activity of Fe^{2+} is mostly affected by dissolution or precipitation of Fe, which varies considerably. Another possible reason for the deviation from equilibrium in most of the Fe-sulphides, as well as the previously discussed Fe-bearing silicates, could be due to the high Fe content in some of the well discharge that is, in some cases, recorded in high content in condensate samples that might be a result of analytical uncertainties. Moreover, a possible cathodic corrosion of the casing material cannot be discounted as a likely cause of the elevated Fe contents in the discharged fluids and, hence, the scatter in the selected samples.

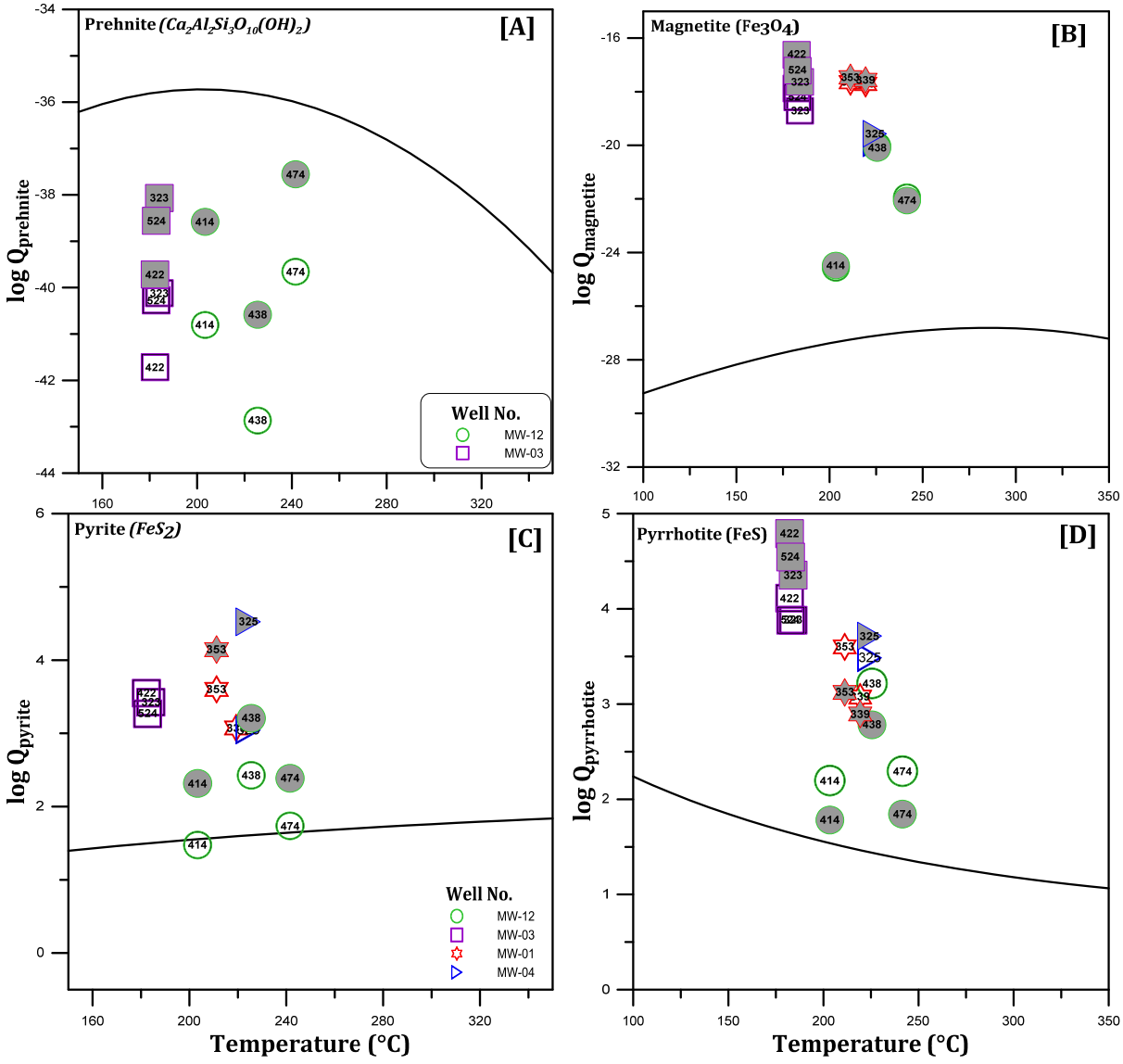

FIGURE 6: Saturation state of Menengai aquifer waters with respect to prehnite (A), magnetite (B), pyrite (C) and pyrrhotite (D); Model 1: unshaded symbols; Model 2: shaded

5.4 Feldspar saturation state

In Menengai, both sanidines and plagioclases occur as the major groundmass component as well as phenocrysts, while albite is the secondary mineral from the feldspars (Kipchumba, 2013; Mibei, 2012). The saturation state of pure Na, K feldspars solubilities in aquifer waters was reconstructed, based on the two models, and is presented in Figure 7. The results show that the water from wells MW-12 and MW-03 are close to super-saturation with respect to low and high albite and microcline and sanidine with a few data points showing a very slight deviation. The high dissolved CO_2 in the aquifer waters may enhance feldspar dissolution since its solubility is pH dependent, thus might lead to super-saturation. The saturation state of the feldspars generally might have been affected by Al analysis and the calculation of the $Al(OH)_4^-$ activity.

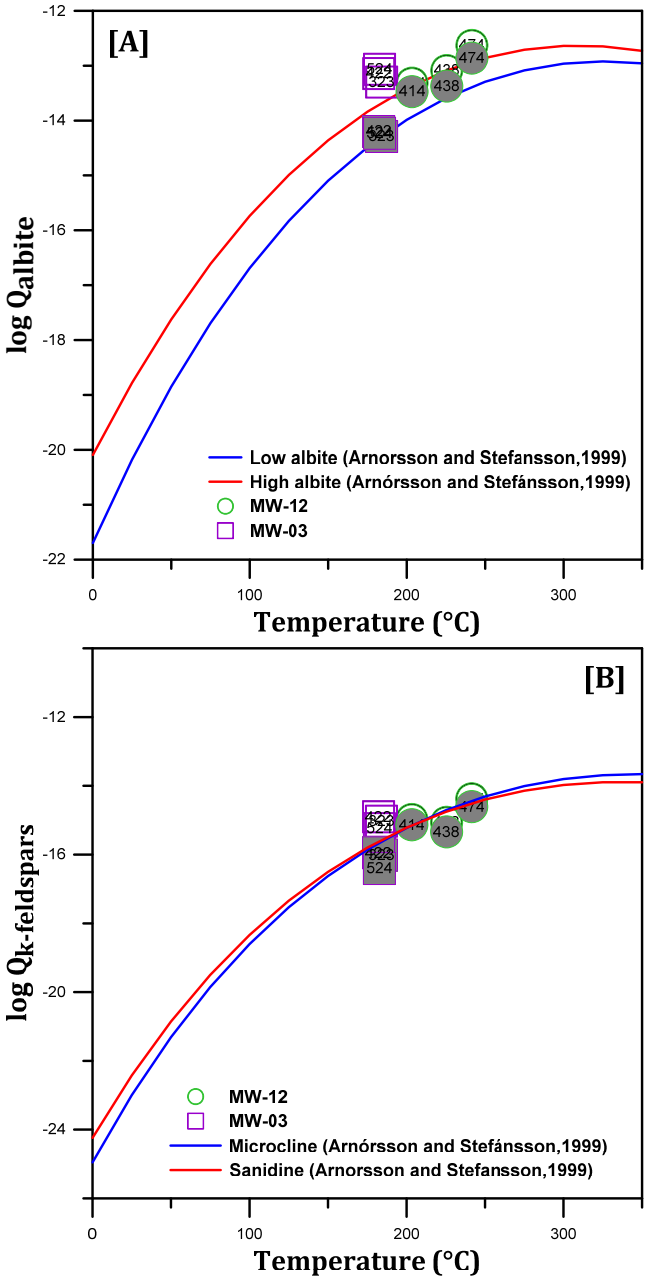

FIGURE 7: The saturation state of end-member feldspars as a function of temperature for pure albite (A) and K-feldspars in Menengai aquifer waters (B)

On the other hand, anorthite is under-saturated in Menengai aquifer waters, as marked by the departure from equilibrium (Figure 1 in Appendix II). Stefánsson and Arnórsson (2000) observed that the saturation state of anorthite in natural waters is somewhat different from that of albite and K-feldspars. The activity ratio of $Ca^{2+}/\sqrt{H^+}$, which is a function of temperature in geothermal waters, controls the aqueous concentration of calcium which is dependent on mineral (epidote, prehnite, and quartz) equilibrium. In addition, the under-saturation of anorthite could also be attributed to the earlier explained highly dissolved CO_2, pH discrepancy and low Ca+ content which have an effect on the activity ratio of $Ca^{2+}/\sqrt{H^+}$. Analytical uncertainties of Al, Ca, and SiO_2 as well as calculation of the $Al(OH)_4^-$ activity might affect the saturation state of feldspars. To eliminate the effect of the analytical uncertainties of Al and aqueous SiO_2, the Na^+/K^+ activity was computed while considering the simultaneous equilibrium of the feldspars.

Na+/K+ activity ratio versus temperature (Figure 2 in Appendix II) corresponds well with the simultaneous equilibrium of low albite/microcline for temperatures above 200°C, typical of well discharges that are approaching dry steam, and high albite/sanidine for temperatures below 200°C. It has been suggested that the Na^+/K^+ activity ratio in geothermal waters is controlled by equilibrium between solution and low albite and microcline when temperatures exceed 200°C (Stefánsson and Arnórsson, 2000).

5.5 Volatile mineral buffers CO_2, H_2S and H_2

The equilibrium curves of mineral assemblages that could potentially control the activities of the main reactive gases CO_2, H_2S, H_2 were compared with that of the calculated dissolved gas concentrations. The results for both models are shown in Figure 8.

For CO_2, the activities of CO_2(aq) in the reservoir water are calculated to be much higher, assuming a liquid only reservoir (i.e. Model 1), whereas the CO_2(aq) concentrations are lower when assuming reservoir vapour to be present together with the liquid water. The reason for this has to do with two things: first, the calculated reservoir pH values are lower in the case of liquid only reservoirs, resulting in higher calculated activities of CO_2(aq); second, assuming reservoir vapour to be present, a considerable fraction of the CO_2 enters the vapour phase, decreasing the total dissolved CO_2 concentration in the liquid phase, as well as the activities of aqueous CO_2(aq). Similar trends were observed with respect to H_2S.

With respect to CO_2(aq), the reservoir fluids, assuming no reservoir vapour to be present (Model 1), results in excess CO_2 compared to possible mineral buffer equilibrium values. However, assuming a reservoir vapour fraction to be present, conditions close to equilibrium were observed. The same is true for H_2S except the difference between the two models was insignificant, i.e. calculated H_2S(aq) concentrations were close to those predicted by mineral buffer reactions.

With respect to H_2, the results are different. Assuming a liquid only reservoir, calculated reservoir H_2 concentrations were orders of magnitude higher compared to when assuming two-phase reservoirs, i.e. liquid and vapour phases. The reason for this is that H_2 is very insoluble. Upon initial boiling (vapour formation), H_2 will quantitatively enter the vapour phase, resulting in very low concentrations of H_2 in the boiled water; in turn, in two phase reservoirs all the H_2 is within the vapour phase. The measured H_2(aq) concentrations for both models were somewhat out of equilibrium with respect to common mineral buffers. This may, in fact, be an artefact

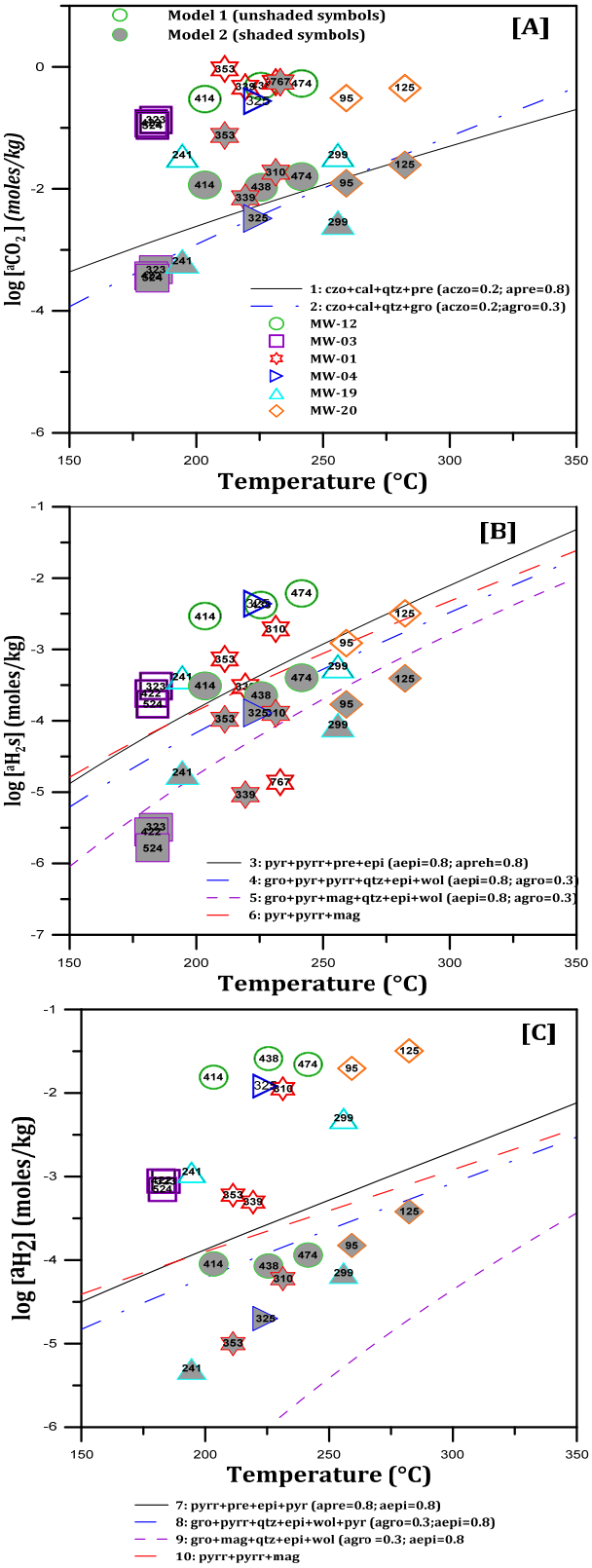

FIGURE 8: State of equilibrium between dissolved CO_2 (A), H_2S (B) and H_2 (C) in the aquifer waters of Menengai wells with several mineral assemblages

related to the assumptions made when calculating the reservoir fluid composition from samples collected at the well-head.

These factors need to be considered when assessing the source of volatile gases in the geothermal reservoir. In fact, calculated excess reservoir gas concentrations relative to mineral buffer reactions, like that observed for CO_2 and H_2, may be the consequence of the model being applied while calculating the reservoir fluid composition rather than true observation. Formation of vapour, either in the reservoir upon heat addition or because of phase separation of liquid water and vapour, may be of importance when making reservoir fluid calculations.

6. THE CAUSE OF EXCESS ENTHALPY

The cause of calculated excess reservoir gas concentration and excess discharge enthalpy may be the result of the same process. For the calculations of reservoir composition, it was assumed that the system was isolated, i.e. no exchange of either matter or energy could take place from the reservoir to the sampling condition. Boiling in natural geothermal systems may, however, not be isolated as heat from hot rock or magma may induce boiling (closed system). Also, the density of the vapour is much less than liquid water; therefore, depending on the hydrological nature of the system, phase separation (open system), either full or partial, may take place (Arnórsson et al., 2007; Scott et al., 2014). As pointed out by Scott et al. (2014), the latter process may be studied by looking at the concentration of a non-volatile like Cl in the liquid phase discharge and the total discharge as a function of the discharge enthalpy. A plot of this for the geothermal well discharges in Menengai geothermal system is shown in Figure 8. As observed, the Cl concentration in the total discharge decreases with increasing enthalpy. On the other hand, the Cl concentration in the liquid phase is relatively constant between 600-1000 ppm and does not increase significantly with increasing enthalpy.

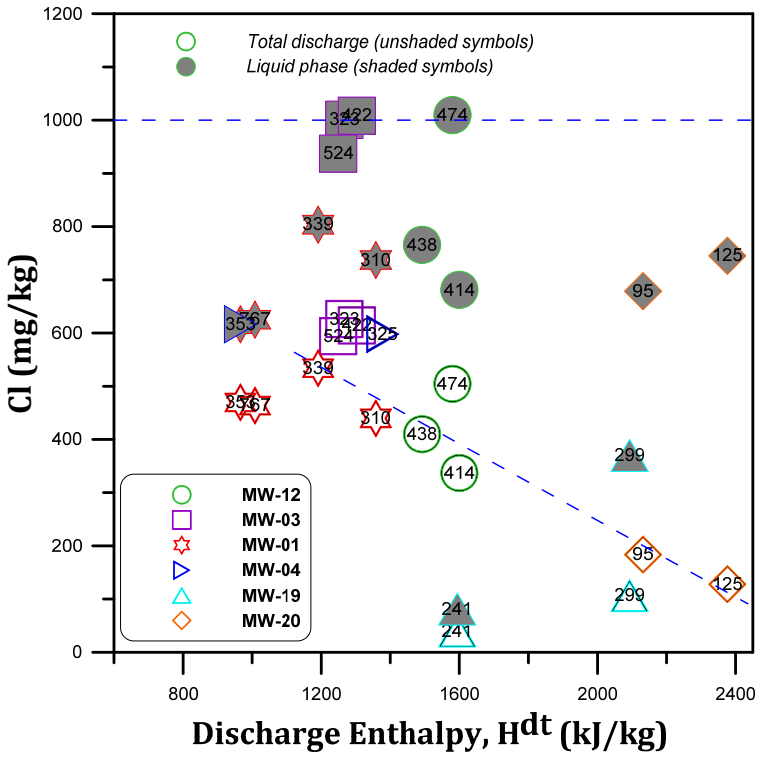

FIGURE 9: The concentrations of Cl in the liquid phase and total two-phase discharge as a function of discharge enthalpy ($H^{d,t}$)

Assume the excess enthalpy is caused by heat addition to the fluid to induce boiling. Such a process would result in increased enthalpy, constant Cl concentration in the total discharge with increasing enthalpy but a sharp increase in the liquid phase Cl concentration with increasing enthalpy. On the other hand, excess enthalpy caused by phase segregation results in a relatively constant Cl concentration in the liquid phase as a function of increased enthalpy, whereas the Cl concentration in the total discharge decreases with increasing enthalpy. As observed in Figure 9, the latter seems to be the case at Menengai, pointing towards phase segregation being the cause of excess enthalpy. Similar conclusions have been drawn for the Olkaria system and many geothermal systems in Iceland (Karingithi et al., 2010; Scott et al., 2014). Moreover, a keen inspection of Figure 9 also depicts a sharp

increase in Cl concentration in the liquid phase with an increase in enthalpy (wells MW-04, MW-01, and MW-03 and partly MW-12). On the other hand, a constant Cl concentration in the total discharge with increasing enthalpy (wells MW-03 and MW-04) was also observed. Therefore, this fits the model of conductive heat transfer from intrusions or magma to the circulating fluids to induce boiling, thus contributing to the excess enthalpy and even forming superheated steam. The remarkably high bottom-hole temperatures and conductive profiles in most wells may substantiate these chemical observations. On a similar note, GAB (2013) postulated the presence of a conductive layer that separates the magma from the zone of superheated steam.

7. CONCLUSIONS

- Two models were adopted in calculating aquifer fluid composition and aqueous species distribution for selected water and steam samples from Menengai wells. The first model assumes a liquid-only reservoir where calculated enthalpy corresponding to equilibrium aquifer temperature was used. The second model considers a liquid and vapour reservoir, where measured enthalpy was used. The calculated chemical composition of major non-volatile components is relatively unaffected by the model used to calculate the reservoir fluid composition; the exception to this is when the well discharges approach dry steam. On one hand, the concentration of the volatiles in reservoir water is significantly lower, assuming a liquid and vapour reservoir, but higher assuming a single-phase liquid reservoir. In principle, the former is attributed to the preferential partitioning of the volatile components into the vapour phase, consequently leading to low H_2S geothermometer temperatures.

- There is a remarkable discrepancy in the calculated geothermometer temperatures, except for well discharges that approach dry steam, typically due to mixing of fluids from different feed zones; nonetheless, the estimated temperature is in excess of 200°C which could correspond to a sub-boiling zone. However the mixing of fluids may affect the fluid equilibrium at a given temperature.

- The saturation state of individual minerals depends on the model-type adopted, thermodynamics, pH and elemental concentration and the stoichiometry of the reaction. The SI values calculated in both models yield under-saturation of all the Ca-bearing as well as pH dependent minerals. This could be caused by removal of Ca from the solution by calcite precipitation in the depressurization zone around wells that might be exacerbated by the high dissolved CO_2 that buffers the pH. The exception to this is with andradite and epidote, both of which show under-saturated and oversaturated conditions in both models. The minerals contain Fe (III) and could be due to overestimation of $Fe(OH)_4^-$ activity. On the other hand, Fe (II) bearing minerals are oversaturated, although this might be affected by the calculated Fe^{2+} activity that is sensitive to precipitation and dissolution. The aquifer waters at temperatures above 200°C have closely approached equilibrium with respect to low-albite and microcline, while at temperatures below 200°C the waters have closely approached equilibrium with high-albite and sanidine.

- The activity of volatiles in the aquifer water in relation to mineral buffers is also model-type dependent. Therefore, activities of volatiles are close to equilibrium with volatile mineral buffers when assuming two-phase reservoir fluids while a departure is observed when assuming a liquid reservoir. Therefore, an unambiguous conclusion on the mineral assemblages that control the concentration of volatile components cannot be ascertained due to the uncertainty attributed to the model calculations as well as to the sensitivity of the reactive gases to the phase separation process.

- The wells drilled in the boiling aquifers of the Menengai geothermal system yield excess enthalpy. Therefore, the trend displayed by the non-volatile Cl concentration in the total well discharge and in the liquid phase as a function of discharge enthalpy suggests that Menengai has a heterogeneous reservoir, with excess enthalpy predominantly caused by partial or full phase separation, with significant contributions from heat transfer from hot rock or magma compounding to form superheated steam in certain wells. It is inherently critical to take into account phase segregation, conductive heat addition and other processes leading to excess enthalpy while calculating reservoir composition since the concentration of volatile components is sensitive to such processes.

ACKNOWLEDGEMENTS

I would like to thank all who, in one way or another, contributed to the success of this course. I would like to express my gratitude to the Government of Iceland and the United Nations University Geothermal Training Programme's (UNU-GTP) current director, Mr. Lúdvík S. Georgsson, for giving me the opportunity to take part in the six months course. I would also like to thank Geothermal Development Company (GDC) for granting me the precious chance and time to undertake this noble training.

I am so grateful to the entire UNU-GTP staff: Dr. Ingvar Birgir Fridleifsson, former UNU-GTP director, Mr. Ingimar G. Haraldsson, Ms. Málfrídur Ómarsdóttir, Ms. Thórhildur Ísberg, Ms. María Gudjónsdóttir and Mr. Markús A.G. Wilde, for their guidance, time and help in various capacities that made the whole training successful. Special thanks also go to Ms. Rósa S. Jónsdóttir, for availing reference material at a time when I needed them.

I am greatly indebted to my supervisor, Prof. Andri Stefánsson of the University of Iceland, for his patience and time in guiding me throughout the project period. The impacted knowledge is greatly appreciated. I would also wish to thank Thráinn Fridriksson for his productive contribution on the chemistry of thermal fluids.

I would finally like to thank the 2014 UNU-GTP fellows, most specifically those who specialised in field of chemistry of thermal fluids, for the memorable moments, the candid friendship and productive critics.

Finally, I give thanks to God for the sufficient grace, divine favour and blessings upon my life.

REFERENCES

Arnórsson, S. (ed.), 2000: *Isotopic and chemical techniques in geothermal exploration, development and use. Sampling methods, data handling, and interpretation*. International Atomic Energy Agency, Vienna, 351 pp.

Arnórsson, S. and Stefánsson, A., 2005: Wet-steam well discharges. II. Assessment of aquifer fluid compositions. *Proceedings of the World Geothermal Congress*, *Antalya, Turkey,* 11 pp.

Arnórsson, S., and Stefánsson, A., 1999: Assessment of feldspar solubility constants in water in the range 0-350°C at P_{sat}. *Am. J. Sci., 299,* 173-209.

Arnórsson, S., Sigurdsson, S. and Svavarsson, H., 1982: The chemistry of geothermal waters in Iceland I. Calculation of aqueous speciation from 0°C to 370°C. *Geochim. Cosmochim. Acta, 46,* 1513-1532.

Arnórsson, S., Stefánsson, A., and Bjarnason, J.Ö., 2007: Fluid-fluid interaction in geothermal systems. *Reviews in Mineralogy & Geochemistry*, 65, 229-312.

Arnórsson, S., Bjarnason, J.Ö., Giroud, N., Gunnarsson, I., and Stefánsson, A., 2006: Sampling and analysis of geothermal fluids, *Geofluids*, *6,* 203-216.

Arnórsson, S., Gunnarsson, I., Stefánsson, A., Andrésdóttir, A., and Sveinbjörnsdóttir, Á.E., 2002: Major element chemistry of surface- and ground waters in basaltic terrain, N Iceland I. Primary mineral saturation. *Geochim. Cosmochim. Acta* 66, 4015–4046.

Arnórsson, S., Angcoy, Jr., E.C., Bjarnason, J.Ö., Giroud, N., Gunnarsson, I., Kaasalainen, H., Karingithi, C., and Stefánsson, A., 2010: Gas chemistry of volcanic geothermal systems. *Proceedings World Geothermal Congress 2010, Bali, Indonesia*.

Bjarnason, J.Ö., 2010*: The chemical speciation program WATCH, version 2.4*. ISOR - Iceland GeoSurvey, Reykjavik, Iceland. Accessible at webpage: *www.geothermal.is/software.*

ELC, 2013: *Provision of consultancy services for the feasibility study for 90 MW Menengai Geothermal Power Project*. Preliminary reservoir capacity report, GDC unpublished report.

Fournier, R.O., 1991: Water geothermometers applied to geothermal energy. In: D'Amore, F. (coordinator), *Application of Geochemistry in Geothermal Reservoir Development*. UNITAR/UNDP publication, Rome, 37-69.

Fournier, R.O., and Potter, R.W. II, 1982: A revised and expanded silica (quartz) geothermometer. *Geoth. Res. Council Bull., 11-10*, 3-12.

Freedman, A. J.E., Bird, D.K., Arnórsson S., Fridriksson, T., Elders, W.A., and Fridleifsson, G. Ó., 2010: Hydrothermal mineral record CO_2 partial pressures in Reykjanes Geothermal System, Iceland. *Proceedings of the World Geothermal Congress 2010, Bali, Indonesia*.

GAB, 2013: *Report of the geothermal advisory board*. Complete draft report, GDC, Kenya, unpublished internal report.

GDC, 2014: *Interpretation of gravity and magnetics data from the Menengai geothermal field.* GRA gravity and magnetic preliminary study project report, GDC, Kenya, unpublished internal report.

Geotermica Italiana Srl., 1987: *Geothermal reconnaissance survey in the Menengai-Bogoria area of the Kenya Rift Valley*. UN (DTCD)/ GOK.

Gichira, J.M., 2012: Joint 1D inversion of MT and TEM data from Menengai geothermal field, Kenya. Report 11 in: *Geothermal Training in Iceland* 2012. UNU-GTP, Iceland, 137-167.

Giggenbach, W.F., 1988: Geothermal solute equilibria. Derivation of Na-K-Mg-Ca geoindicators. *Geochim. Cosmochim. Acta, 52*, 2749-2765.

Gudmundsson, B.T., and Arnórsson, S., 2005: Secondary mineral-fluid equilibria in the Krafla and Námafjall geothermal systems, Iceland. *Applied Geochemistry, 20,* 1607-1625.

Gunnarsson, I. and Arnórsson S., 2000: Amorphous silica solubility and the thermodynamic properties of $H_4SiO_4°$ in the range of 0° to 350°C at P_{sat}. *Geochim. Cosmochim. Acta, 64*, 2295-2307.

Kahiga, E.W., 2014: Borehole geology and hydrothermal alteration mineralogy of well MW-13, Menengai geothermal field, Kenya. Report 16 in: *Geothermal Training in Iceland* 2014. UNU-GTP, Iceland, 261-294.

Karingithi, C.W., Arnórsson, S., and Grönvold, K., 2010: Processes controlling aquifer fluid compositions in the Olkaria geothermal system, Kenya. *J. Volc. Geothermal Res.196*, 57-76.

Kipchumba, L, J., 2013: Borehole geology and hydrothermal alteration of wells MW-08 AND MW 11, Menengai geothermal field, Kenya. Report 10 in: *Geothermal Training in Iceland* 2013. UNU-GTP, Iceland, 143-176.

Kipng'ok, J., 2011: Fluid chemistry, feed zones and boiling in the first geothermal exploration well at Menengai, Kenya. Report 15 in: *Geothermal Training in Iceland* 2011. UNU-GTP, Iceland, 281-302.

Lagat, J., Mbia, P., and Muturia, C., 2010: *Menengai prospect: Investigations for its geothermal potential.* GDC, Kenya, internal report, 64 pp.

Leat, P.T., 1984: Geological evolution of the trachytic caldera volcano Menengai, Kenya Rift Valley. *J. Geological Society, 141*, 1057-1069.

Lopeyok, T.P., 2013: Borehole geology and hydrothermal mineralization of wells MW-09 AND MW -12, Menengai geothermal field, Kenya. Report 15 in: *Geothermal Training in Iceland* 2013. UNU-GTP, Iceland, 289-324.

Malimo, S.J., 2013: Fluid chemistry of Menengai geothermal wells, Kenya. *Geothermal Resources Council Transactions, 37,* 425-430.

Mbia, P.K., 2014: S*ub-surface geology, petrology and hydrothermal alteration of Menengai geothermal field, Kenya*. University of Iceland, MSc thesis, UNU-GTP, report 1, 87 pp.

Mibei, G.K., 2012: Geology and hydrothermal alteration of Menengai geothermal field – Case study: wells MW-04 and MW-05. Report 21 in: *Geothermal Training in Iceland* 2012. UNU-GTP, Iceland, 437-465.

Mibei, G.K. and Lagat, J., 2011: Structural controls in Menengai geothermal field. *Proceedings of Kenya Geothermal Congress, Nairobi.*

Mungania, J., and Lagat, J., (ed.), Mariita, N.O., Wambugu, J.M., Ofwona, C.O., Kubo, B.M., Kilele, D.K., Mudachi, V.S., Wanjie, C.K., and Korio, R.K., 2004: *Menengai volcano: Investigations for its geothermal potential.* KenGen, Kenya, internal report, 93 pp.

Omondi, C., 2011: Borehole geology and hydrothermal mineralisation of wells MW-01 and MW-02, Menengai geothermal field, Central Kenya Rift Valley. Report 30 in: *Geothermal Training in Iceland* 2011. UNU-GTP, Iceland, 737-773.

Scott, W, S., Gunnarsson, I., Arnórsson, S., and Stefánsson, A., 2014: Gas chemistry, boiling and phase segregation in geothermal systems, Hellisheidi, Iceland. *Geochim. Cosmochim. Acta, 124*, 170-189.

Sekento, L.R., 2012: Geochemical and isotopic study of the Menengai geothermal field, Kenya. Report 31 in: *Geothermal Training in Iceland* 2012. UNU-GTP, Iceland, 769-792.

Simiyu, S.M., 2009: Application of micro-seismic methods to geothermal exploration: Examples from Kenyan rift. Paper presented at *"Short Course IV on Exploration for Geothermal Resources", organized by UNU-GTP, GDC and KenGen, at Lake Naivasha, Kenya,* 27 pp.

Simiyu, S.M. and Keller, G.R., 2001: An integrated geophysical analysis of the upper crust of the southern Kenya rift. *Geophysical J. International, 147,* 543-561.

Stefánsson, A., and Arnórsson, S., 2000: Feldspars saturation state in natural waters, *Geochim. Cosmochim. Acta, 64*, 2567-2584.

UP and GDC., 2013: *Structural characteristics of Menengai Caldera, central Kenya Rift, Republic of Kenya - Preliminary assessment of the structural characteristics of Menengai Caldera and regions farther north.* GDC, Kenya, unpublished internal report.

Wamalwa, A.M., 2011: *Joint geophysical data analysis for geothermal energy exploration*. University of Texas, PhD thesis, El Paso, Texas.

Wamalwa, A.M., Mickus, K.L., and Serpa, L.F., 2013: Geophysical characterization of the Menengai volcano, Central Kenya Rift from the analysis of magnetotelluric and gravity data. *Geophysics, 78*, B187-B199.

APPENDIX I: Geothermometer temperatures

TABLE 1: Geothermometer and measured temperatures for Menengai wells

Well No.	Sample No.	$Tqtz^a$		$Tqtz^b$		$T_{Na/K}{}^a$		$T_{Na/K}{}^b$		T_{H2S}			Measured temperature	
		Model 1	Model 2	Model 1	Model 2	Model 1	Model 2	Model 1	Model 2	Model 1	Model 2	Average^{av}	Depth (m)	Temp (^oC)
MW12	414	206	208	199	201	155	155	168	168	285	220	203	1200	246
	438	227	230	221	225	114	114	129	129	295	212	226	1800	273
	474	242	245	237	242	143	143	156	156	307	227	242	Bottom hole	>320
MW03	323	184	192	176	184	145	145	158	158	220	118	184	1250	155
	422	183	190	174	182	141	141	155	155	214	115	182	1350-1400	172
	524	183	191	174	183	89	89	105	105	205	106	183	Bottom hole	>320
MW01	339	219	226	213	220	191	191	200	200	220	139	219	1051-1346	173-185
	353	214	215	207	208	185	185	195	195	244	193	211	1790/1800*	301/180*
	310	232	236	226	231	164	164	176	176	272	198	231	2000	324
	767	236	236	231	231	153	153	166	166	147	147	233	Bottom hole	>390
MW04	325	223	231	217	226	139	139	153	153	297	198	224	1200-1400 1950 Bottom hole	177 204 >390
MW19	241	198	199	190	191	239	239	244	244	228	154	194	1200, 1450, 2000	212 280, 284
MW19	299	255	259	253	257	145	145	158	158	238	189	256	Bottom hole	>330
MW20	95	259	261	257	260	244	244	248	248	259	205	259	N/A	
MW20	125	278	283	281	287	269	269	271	271	287	227	282		

$Tqtz^a$ according to the geothermometer function of Fournier and Potter (1982) , $Tqtz^b$ according to Gunnarsson and Arnorsson (2000), $T_{Na/K}{}^a$ Fournier (1979), $T_{Na/K}{}^b$ Giggenbach (1988), T_{H2S} based on equation 6 in Table 3, which corresponds to equilibrium between pyrite, pyrrhotite, magnetite and solution. * The measured temperature at a time that somewhat corresponds to that of collecting sample 767 of MW-01. ^{av} Average quartz geothermometer temperature according to the two models

APPENDIX II: Saturation state of aquifer waters of Menengai with respect to minerals

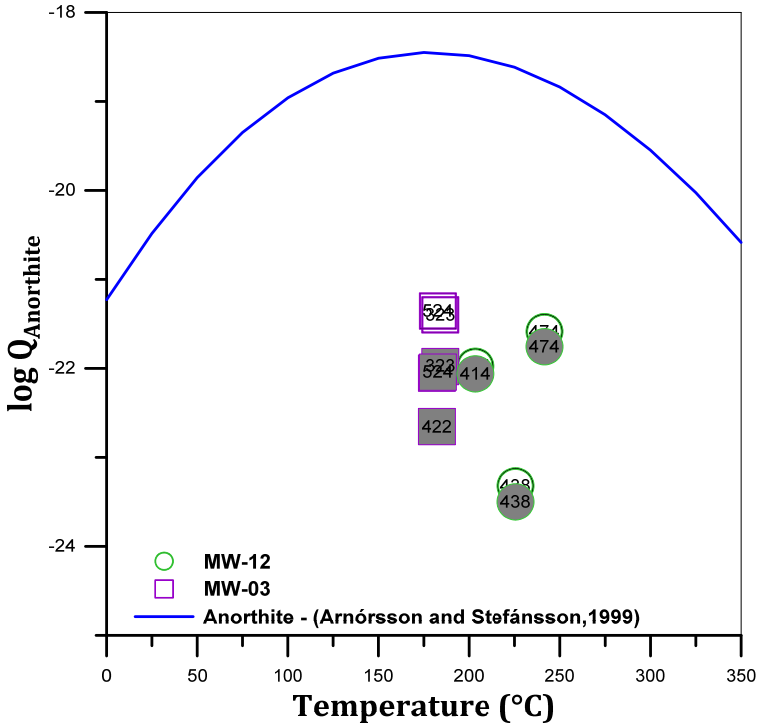

FIGURE 1: The saturation state of end-member feldspars as a function of temperature for anorthite in Menengai aquifer waters

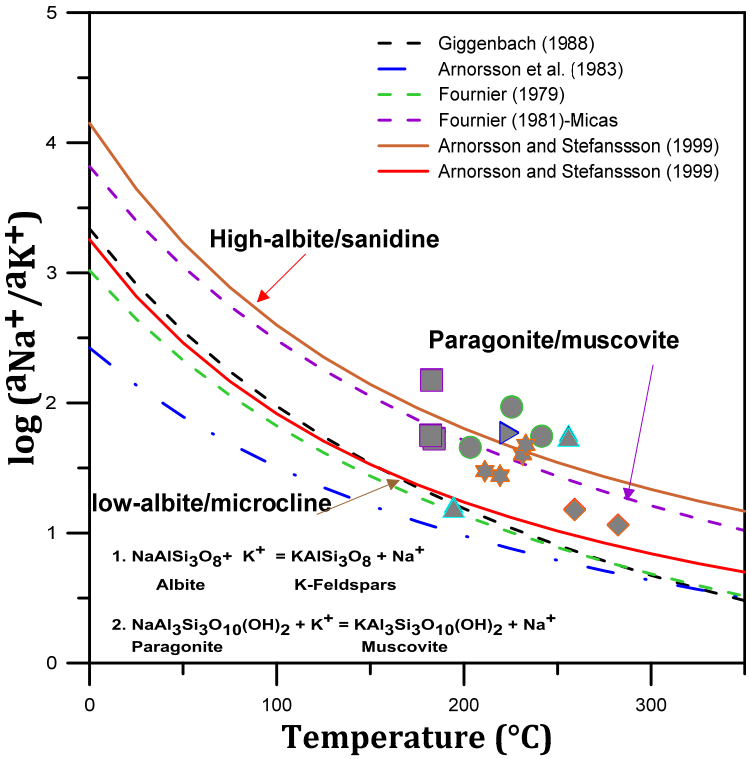

FIGURE 2: Aqueous Na^+/K^+ activity ratios versus temperature